University of Science and Technology of China

A dissertation for bachelor's degree

Modeling and simulation of beam induced backgrounds measured by ATLAS Forward Proton (AFP) detector

Author: Yicong Huang
Department of Modern Physics
Student ID: PB13000327
Supervisor: Tomas Sykora
Finished time: May, 2016

Contents

Abstract

The ATLAS Forward Proton (AFP) detector is a forward detector of the ATLAS experiment at CERN. Its main goal is to trigger diffractive protons in collisions at the Large Hadron Collider (LHC). To achieve this, the detector has to be placed very close to the beam. Inevitable consequence is that its measurements can be easily affected by the beam induced background.

This thesis presents a study of the beam induced background in the AFP detector and discuss methods for its removal. The Geant4 simulations and data, including non-colliding bunches are used to identify characteristic features of beam induced backgrounds. A method using combination of signals detected by the AFP detector and the Minimum Bias Trigger Scintillators (MBTS) is used to selected single diffractive event namely on low pile-up data taken during the first AFP physics run in 2016.

Finally, an estimate of the beam induced backgrounds level in data together with a study of the radiation environment at the AFP stations was made, comparing results with exploitations.

Keywords: AFP, ATLAS, beam halo, simulation.

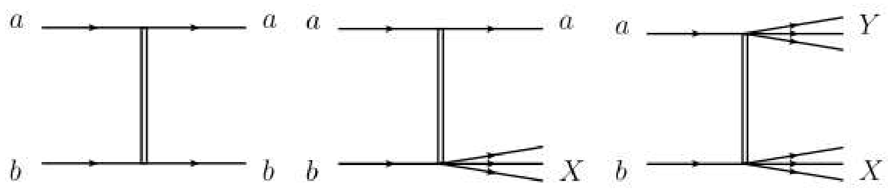

(a) (b) (c)

Figure 1. Feynman diagrams of diffractive processes: (a) elastic scattering, (b) single diffractive dissociation, (c) central diffractive dissociation.

1 Introduction

The ATLAS Forward Proton (AFP) detector aims to measure forward protons that are scattered in the ATLAS interaction point (IP) under very small angles ($< 300\,\mu\mathrm{rad}$). The major processes that can be studied with the AFP detector are diffractive scatterings, where one or two protons remain intact. In such processes, protons interact by exchanging of a colourless object, the so-called Pomeron [1]. In principle, the Pomeron structure should be described in terms of the QCD which represents not closed subject yet.
Several diffractive signatures can be distinguished: if both protons stay intact and no additional particles are produced, one deals with elastic scattering, Fig. 1(a). The interaction when one interacting proton dissociates into multi-particle state, the process is called single diffractive dissociation, Fig. 1(b). Single diffractive processes form about 20% of the total cross section. If both interacting protons dissociate we speak about double diffractive dissociation, Fig. 1(c). It is also possible to have a diffractive interaction with central production of particles. Such processes are called central diffractive or double Pomeron exchange processes, have low cross sections but are of great interest.

The AFP detectors combine the silicon pixel tracker and the high resolution time-of-flight (ToF) detector to achieve the high-precision measurements of the forward protons. The stations are placed at 205 m and 217 m from the interaction point on both sides of the ATLAS central detector. To measure protons with very small scattering angles, the detectors have to be placed very close to the beam center and as such, the beam induced backgrounds [2] in the AFP are much more significant than other parts of the ATLAS detector. It makes the study of the diffractive processes more difficult. The possible sources of beam induced backgrounds in the AFP are

- **Beam halo**: Particles travel together with a bunch for one or many turns before being detected by the AFP. These particles have similar kinematic properties like signal, but do not originate from the IP and should not have an associate process in the main detector.

- **Beam gas**: Beam protons interact with the residual gas inside the beam pipe producing scattered protons or showers that may affect the AFP detectors.

- **IP secondary interactions**: High-energy primary particles produced in the IP may cause interactions upstream of the AFP, and the secondaries (or tertiaries) may reach the AFP detectors.

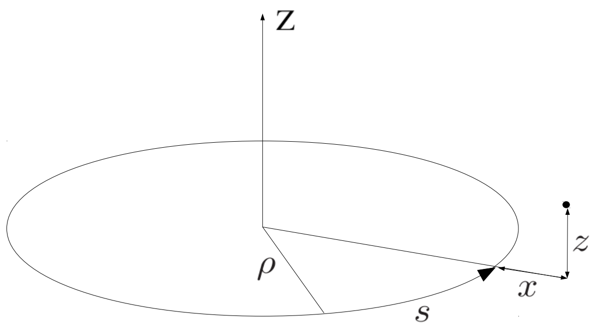

Figure 2. Circular designed orbit and coordinates used to describe particle trajectories. The length of the designed orbit is s. x, z mean the deviations in horizontal and vertical direction. ρ is the radius of the designed orbit.

- **Interaction with the AFP stations**: Protons interact with the AFP stations and products are then detected by the detectors.
- **Backscattering due to collimators after the AFP**: The collimator after the AFP might cause some 'back scattering' into the AFP detectors.

The aim of this study is to estimate the beam induced backgrounds level measured by the AFP detectors. As will be shown, the main source of beam induced backgrounds in the AFP is caused by beam halo. The amount of other kinds of beam induced backgrounds is very small.

2 The LHC Optics

2.1 Transverse Optics

Any kind of circular accelerator has a designed orbit, on which ideally all particles should move. To keep beam particles moving on the designed orbit, bending forces are needed, which are usually provided by dipole magnets. In reality, most particles of the beam will deviate slightly from the designed orbit and to keep these deviations small on the whole way, focusing forces are needed. The focusing forces are usually provided by quadrupole magnets. The coordinates used to describe a circular acelerator are shown in Fig. 2, ρ is the designed radius of the orbit, the position of a particle is described by s, x and z coordinates [3].

2.1.1 The Hill's Equations

The basic equations for describing a particle trajectory [**?**] are

$$x'' - (k - \frac{1}{\rho^2})x = \frac{1}{\rho}\frac{\Delta p}{p_0}, \tag{1}$$

$$z'' + kz = 0, \tag{2}$$

where x, z are the deviations with respect to the ideal designed trajectory, k and ρ are periodic functions of s because the orbit is a closed curve. These equations are called as Hill's equation. In what follows we consider only particles of momentum $p = p_0$, i.e. their momentum loss $\Delta p = 0$.
Then both equations read

$$y'' + K(s)y = 0, \tag{3}$$

$$K(s+L) = K(s). \tag{4}$$

We can express any solution $y(s)$ of the equations in the form

$$y(s) = y_0 C(s) + y_0' S(s), \tag{5}$$

where $C(s)$ and $S(s)$ are two independent solutions of the homogeneous equation

$$C'' + K(s)C = 0, S'' + K(s)S = 0, \tag{6}$$

so $y(s)$ and $y'(s)$ can be obtained from y_0 and y_0' by matrix multiplication

$$\begin{bmatrix} y(s) \\ y'(s) \end{bmatrix} = M(s/s_0) \begin{bmatrix} y(s_0) \\ y'(s_0) \end{bmatrix}, M(s/s_0) = \begin{bmatrix} C(s,s_0) & S(s,s_0) \\ C'(s,s_0) & S'(s,s_0) \end{bmatrix}, \tag{7}$$

with the boundary conditions

$$\begin{bmatrix} C(s_0,s_0) & S(s_0,s_0) \\ C'(s_0,s_0) & S'(s_0,s_0) \end{bmatrix} = \begin{bmatrix} 1 & 0 \\ 0 & 1 \end{bmatrix}. \tag{8}$$

The transfer matrix M has a period L, the matrix between point s and s_0 can be computed by matrix multiplication

$$M(s/s_0) = M(s/s_1) \cdot M(s_1/s_0). \tag{9}$$

We can express M in a very useful form

$$M = I\cos\mu + J\sin\mu. \tag{10}$$

Here I is the unit matrix and $J = \begin{bmatrix} \alpha & \beta \\ -\gamma & -\alpha \end{bmatrix}$, with $\beta\gamma - \alpha^2 = 1$, $\cos\mu = \frac{1}{2}\text{trace } M$. α, β and γ are periodic functions of s with the period L, μ is independent of s.

2.1.2 The Beta Function

The periodic function $\beta(s)$ is called "beta function". To express α through the beta function, consider the eigenvalues of the transfer matrix $M(s+L/s)$

$$\begin{bmatrix} y(s+L) \\ y'(s+L) \end{bmatrix} = M(s+L/s) \begin{bmatrix} y(s) \\ y'(s) \end{bmatrix} = e^{\pm i\mu} \begin{bmatrix} y(s) \\ y'(s) \end{bmatrix}. \tag{11}$$

We obtain

$$y(s)\cos\mu + (y(s)\alpha + y'(s)\beta)\sin\mu = y(s)(\cos\mu \pm i\sin\mu), \tag{12}$$

$$y(s)\alpha + y'(s)\beta = \pm iy, \tag{13}$$

$$\frac{y'}{y} = \frac{\pm i - \alpha}{\beta}. \tag{14}$$

By differentiation of both sides of equation (14) we get

$$\frac{y''}{y'} - \frac{y'}{y} = \frac{-\alpha'}{i - \alpha} - \frac{\beta'}{\beta}. \tag{15}$$

With $y'' = -Ky$ we can get another kind of expression

$$\frac{y''}{y'} - \frac{y'}{y} = -\frac{K\beta}{i - \alpha} - \frac{i - \alpha}{\beta}, \tag{16}$$

so

$$(\alpha^2 + K\beta^2 + \alpha\beta' + \alpha\beta' - \alpha'\beta - 1) - i(2\alpha + \beta') = 0. \tag{17}$$

The elements of M are real, therefore we get pair of equations:

$$\alpha(s) = -\frac{1}{2}\beta'(s), \tag{18}$$

$$\alpha^2 + K\beta^2 + \alpha\beta' - \alpha'\beta - 1 = 0. \tag{19}$$

Using the first equation to eliminate α we obtain the following differential equation for the beta function

$$\frac{1}{2}\beta\beta' - \frac{1}{4}\beta'^2 + K\beta^2 = 1. \tag{20}$$

The solutions of the Hill's equation can also be written in terms of the beta function

$$y(s) = a\sqrt{\beta}\cos(\varPhi - \delta), \tag{21}$$

$$y'(s) = -\frac{a}{\sqrt{\beta}}\big(\alpha\cos(\varPhi(s) - \delta) + \sin(\varPhi(s) - \delta)\big), \tag{22}$$

where $\Phi'(s) = \frac{1}{\beta}$, δ is an arbitrary constant phase depending on the trajectory, it can take any value between 0 and 2π. In the (y, y') plane, if δ varies between 0 and 2π, the point (y, y') moves around an ellipse with an area of $\pi\epsilon$. Instead of the area of the ellipse, the constant $\epsilon = a^2$ (emittance) is more commonly used to describe accelerator optics. Using ϵ we can write

$$y(s) = \sqrt{\epsilon\beta(s)}\cos(\varPhi - \delta). \tag{23}$$

The beam envelope is defined as $y_{max}(s) = \sqrt{\epsilon\beta(s)}$, as shown in Fig. 3.

2.2 Layout of the Forward Region

The Large Hardon Collider (LHC) [4] consists of two separate rings with eight straight sections centered on Interaction Points (IP). The beams collide in four of the IPs: IP1 (ATLAS and LHCf), IP2 (ALICE), IP5 (CMS and TOTEM), IP8 (LHCb and MoEDAL). To keep the beams in their circular paths 1232 dipole magnets are used. Additionally, 392 quadrupole magnets are installed to keep the beams focused [4]. The quadrupole magnets

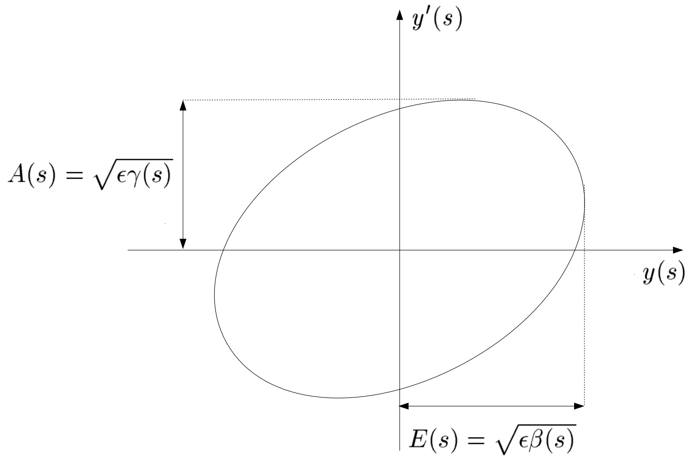

Figure 3. Beam envelope and divergence. [3]

are labelled with the letter Q and the dipole magnets with the letter D. Fig. 4 shows the layout of the ATLAS forward region and the ATLAS coordinates. The IP1 is the zero point in the ATLAS coordinates. The z-axis is along the longitudinal direction and the $x - y$ planes is at the transverse direction. The ATLAS coordinates will be used in the following parts of the thesis. The final focusing triplet (Q1, Q2, Q3) is positioned about

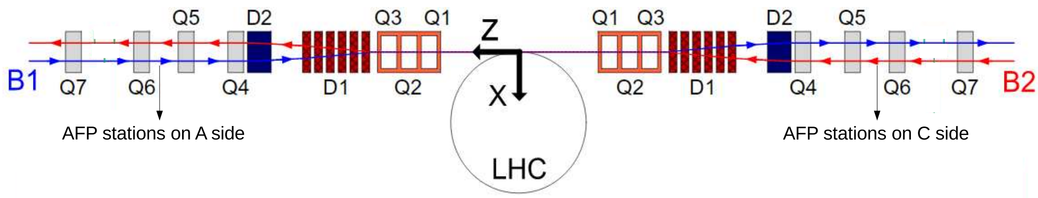

Figure 4. Layout of the forward region. The left side of this picture is called as "A" side, the right side is called as "C" side. The AFP stations are installed between Q5 and Q6.

40 m away from the IP1. Other quadrupoles (Q4, Q5, Q6) are installed around 160 m, 190 m and 220 m from the ATLAS IP. Between the IP1 and 210 m two dipole magnets, D1 at 70 m and D2 at 150 m, are installed. These magnets are used for the separation of ingoing and outgoing beams [5].

To protect the detector and suppress beam halo, several collimators are installed. Fig. 5 shows a collimator model and a photo of a collimator taken during the AFP installation. A collimator has two jaws to limit the size of a beam, the beam goes through the gap between the two jaws so that collimators limit the size of the beam by setting the width of the gap between two jaws. The jaws are the top blue parts in the model in Fig. 5. We use "outer" to indicate the collimator jaw which is farther from the LHC ring center, "inner" to indicate the collimator jaw which is closer to the LHC ring center. There are two collimators between the IP1 and the AFP stations, TCL4 and TCL5. Collimator TCL4 is located at 150.53 m, with the outer jaw opened to 8.57 mm and the inner jaw opened to

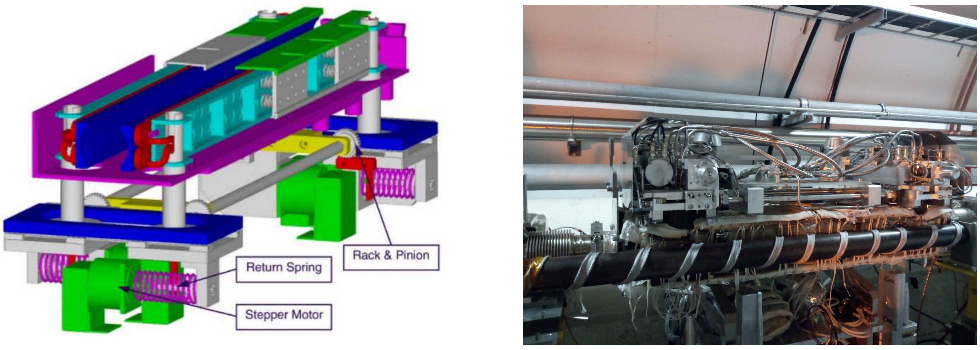

Figure 5. Model of a collimator [6] (left), and the photo of collimator TCL6 taken during the AFP installation (right).

10 mm. Collimator TCL5 is located at 184.857 m with its outer jaw opened to 10.96 m and inner jaw opened to 12.51 m [7]. Beside TCL4 and TCL5, another collimator that can affect the AFP detector is TCL6. Collimator TCL6 is located at 223.232 m from the IP1, after the AFP stations but very close to the stations, so it could cause some shower particles upstream to the AFP stations. The locations available to the AFP are at distances along the beam line between 204 m and 217 m from the ATLAS IP on both sides. The full AFP program includes four stations, two on the left side of the IP1 and two on the right side of the IP1. Stations on the right side are placed at 205.217 m and 217.302 m from IP1 along the z-axis, stations on the left side are placed at 205.823 m and 217.908 m from the IP1 along the z-axis, between Q5 and Q6. The outer side of the beam was chosen as the side to put the AFP stations so the main collimator jaw which has effect is the outer jaw. We use ”C side” to denote the right side of IP1, ”A side” to denote the left side of IP1, as shown in Fig. 4. The stations closer to the IP are called as near stations, the farther stations are called as far stations. The AFP stations on C side were installed during winter 2015 - 2016 shutdown, but the Time-of-Fligh (ToF) detector in the far station was not installed. This setting was the so-called AFP ”0+2” configuration. The other two stations on the A side were installed during March in 2017, in the stations on the C side tracker detectors were replaced, ToF detectors were installed on both side. The final configuration is called as the AFP ”2+2”.

2.3 The LHC Optics for AFP Runs

The optics used in the first part of 2016 data taking starting from the first AFP beam based alignment (BBA) run, till run 301795. This includes the first AFP physics run: Run 305359, taken in August of 2016. The designed beam parameters are listed in Table 1.

The designed crossing angle of the beam is 185 $\mu\mathrm{rad}$ in the optics used in the first part of 2016 data taking, as shown in Fig. 6. Beam 1 enters ATLAS side A with positive and leaves side C with negative y position value, beam 2 enters ATLAS side C with positive and leaves side A with negative y position value. Fig. 7 shows the positions of different proton trajectories got from simulation.

The upper plots in Fig. 6 are $x - z$, $y - z$ distributions of trajectories with different beam energy but $p_T = 0$. From the $x - z$ distribution we know that the more energy a

Name	IP1	Near C	Far C
β_x[m]	0.4	80.46	23.20
β_y[m]	0.4	656.84	487.93
$\epsilon[\mu m]$	3.5		
$\sigma_{x'}^{nom}[\mu rad]$	35.54	2.51	2.51
$\sigma_{y'}^{nom}[\mu rad]$	35.54	0.88	1.02
$\sigma_{x}^{nom}[\mu m]$	14.2	202	108
$\sigma_{y}^{nom}[\mu m]$	14.2	577	497

Table 1. List of the designed beam parameters. [7]

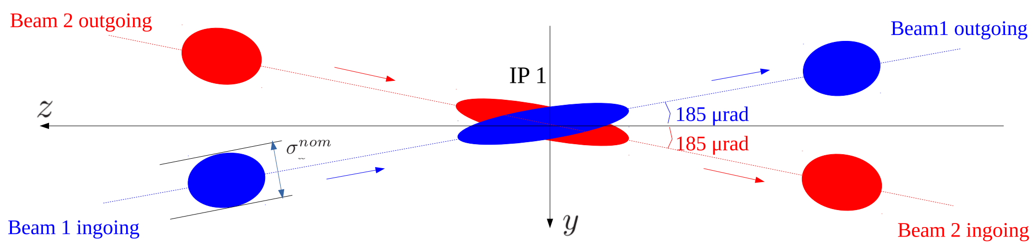

Figure 6. Crossing angle and beam parameter σ at the IP1.

proton loses, the farther it will go on x. The middle plots are $x-z$, $y-z$ distributions of trajectories with different p_x but E = 6500 GeV and $p_y = 0$. By comparing the $x-z$ distributions for different energy and different p_x, it is clear that energy loss has much more effect on the position of the proton.
The bottom plots are $x-z$, $y-z$ distributions of trajectories with different p_y, but E = 6500 GeV and $p_x = 0$. The beam center at the near station is at x = -97.0 mm, y = -3.0 mm and at x = -97.0 mm, y = -2.6 mm at the AFP far station when used the optics described here.

3 The AFP Detector

3.1 Detector Components

Each of the AFP stations is composed by the Roman Pot (RP) and the Silicon pixel Tracker (SiT), far stations contain also ToF detectors for rejecting pile-up at high luminosity. The SiT and the ToF detectors are installed in the Roman Pot as shown in Fig. 8. The plate in this picture is the Roman Pot flange, the vertical direction is the y-axis, the direction perpendicular to the flange is the x-axis.

3.1.1 The Roman Pot

The Roman Pot was selected as the AFP beam interface. The starting point for the AFP RP design is the TOTEM cylindrical pot [8], which was produced by CERN and fully

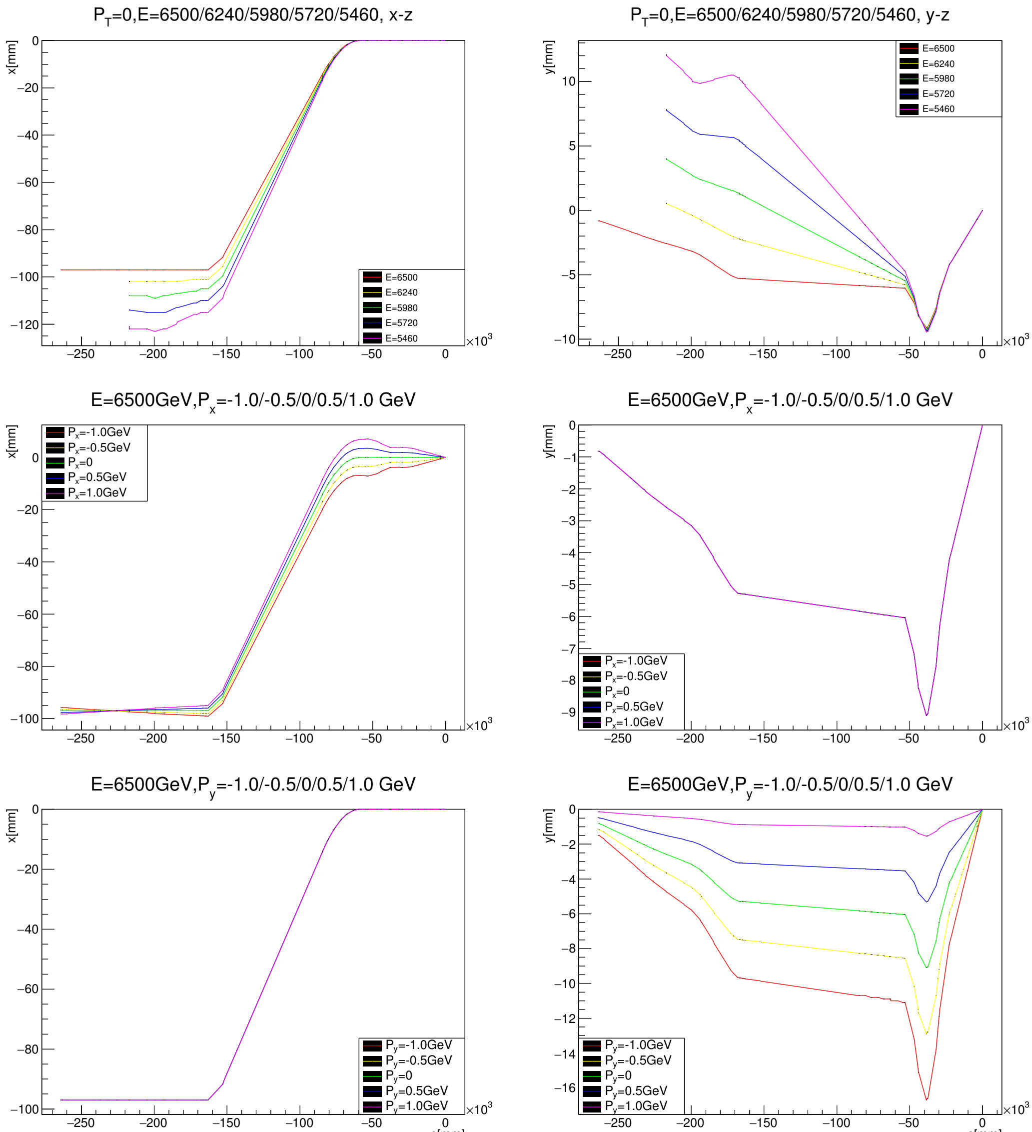

Figure 7. Proton trajectories for different energy (upper), p_x (middle) and p_y (bottom) based on simulation. The x-axis is s, the y-axis is the x (left) or y (right) positions in the ATLAS coordinates, in the unit of mm.

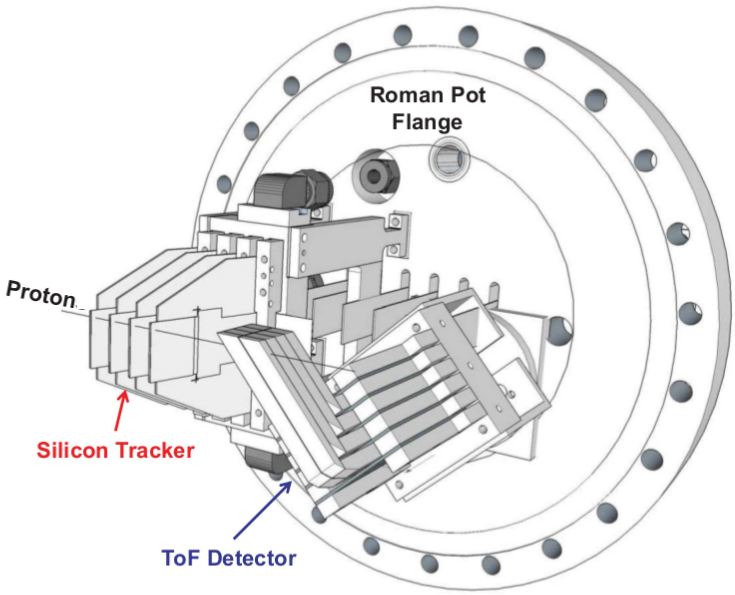

Figure 8. The model of an AFP station with an example of a passing proton.

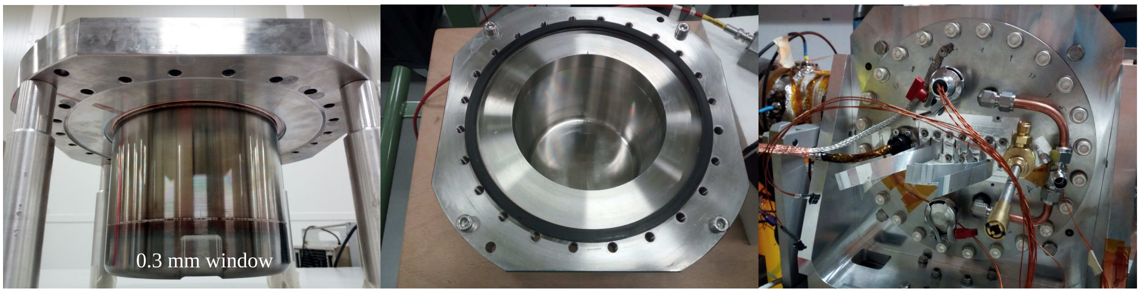

Figure 9. The Roman Pot with the 0.3 mm window (left), the inside part of a pot (middle), the Roman Pot flange (right).

qualified for using in the tunnel. However, the TOTEM RP design is not well suited for the AFP ToF detector, because the AFP ToF requires a $50\ \mathrm{mm} \times 50\ \mathrm{mm}$ flat area on the RP bottom interfacing between the quartz Cerenkov radiators and the LHC beam vacuum. Also, the AFP silicon tracker sensor is 20.0 mm wide in y.
The material of the pot, as for many LHC beam elements, is type 316LN stainless steel [9], a low-carbon, nitrogen-enhanced version of Type 316 molybdenum-bearing austenitic stainless steel. The design of the Roman Pot is shown in Fig. 9. As shown in the left picture, the RP floor has a 0.3 mm thin window which was machined by removing a 1.7 mm thick and 20 mm wide layer of material from the 2.0 mm thick bottom and wall of the cup. The window is used as the interface of the beam and the detector. A Roman Pot has two major components, a pot and a precision feed-through plate. The plate is used to close the pot and provide holes for the feed-through connections.
Feed-through connections on the Roman Pot flange including low voltage, high voltage for the SiT, connectors between the sensors and the read-out electronics, high voltage for the ToF, temperature sensors, vacuum pump tubes and the cooling system. The vacuum inside the pot is provided by the LHC beam pipe vacuum pump. Because of the secondary vacuum, the electronics inside the pot needs cooling. The cooling system receives cold air from a Dry Air Vortex Cooling system [13], the cold air goes through the heat exchanger, then goes out from the longest tube shown in the right picture in Fig. 9. Such system can easily cool the Roman Pot and the detectors.

3.1.2 The Silicon Tracker

To measure diffractive protons, the AFP detectors must be able to approach the beam closely, so the radiation at the AFP stations is higher than at the location of the first layer of the ATLAS inner tracker. The required resolution needed for physics analysis is $10\ \mu\mathrm{m}$ in the x direction.
Because of the above requirements, the AFP baseline tracker device is the 3D silicon pixel tracker, used for the ATLAS Insertable B-Layer (IBL) tracker [10]. In addition, the choice of the 3D sensor allows the use of the well-tested FE-I4B front-end chip [11] and indicates the use of the RCE-based DAQ system [12] used extensively for the 3D sensor testing.
Each AFP station contains one SiT, the configuration listed below is the designed configuration of the detector and it was used in full GEANT4 simulation (Sect. 3.2).

- The SiT has four layers, separated by 9 mm along the z-axis, rotated by $14°$ around the y-axis (viz Fig. 10). In the configuration in 2016, the SiT in the near station had only three layers.

- Each layer has a silicon pixel sensor with thickness of 230 $\mu\mathrm{m}$, contains an array of 336×80 pixels of size $50 \times 250\ \mu\mathrm{m}^2$. Each sensor is bonded with a FE-I4B read-out chip with thickness of 700 $\mu\mathrm{m}$.

- The sensor is hold by a plate with thickness of 1 mm, length of 44 mm, width (along the y-axis) of 58 mm. The material of the plate is Al-Cf (60% C, 40% Al). Except holding the sensor, the plates also work as heat exchanger for the sensors.

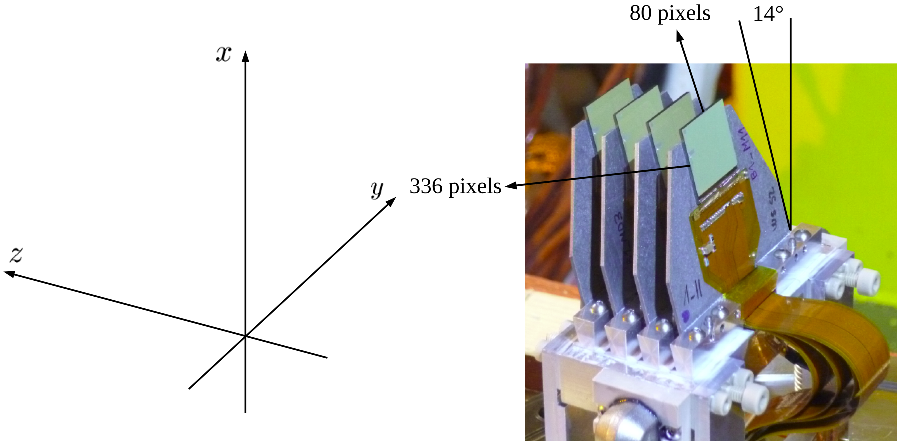

Figure 10. 3D silicon sensors mounted on the plates and its coordinate system.

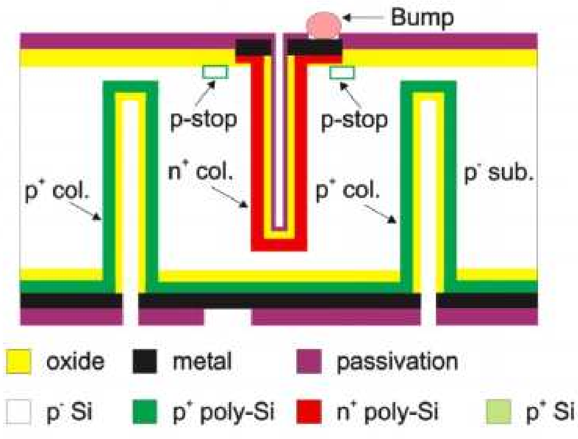

Figure 11. Details of a sensor layout. [13]

- The designed distance from the edge of the sensor to the beam center on the x-axis is 15 σ_x^{nom}, here σ_x^{nom} is the x-size of beam envelope at the AFP station. The y-position of the stations are designed to be at the center of the beam pipe, which is y = 0 mm in the ATLAS coordinates. In the configuration in 2016, the distance from the RP edge to the beam center in the near station was 4.04 mm, in the far station was 2.16 mm. The stations did not arrive at 15 σ_x^{nom} from the beam center in 2016.

The silicon sensor is attached to the plate as shown in Fig. 10. The rectangle on the top of each plate is the sensor bump-bonded (connected) to a FE-I4B front-end chip. The active area of the sensor is $16.8 \times 20.0\,\mathrm{mm}^2$, beside of the active area, each sensor has a 180 $\mu\mathrm{m}$ dead edge at the side facing the beam. The pixels are p-type Si, with a very high resistivity (10 to 30 kΩ cm). Each pixel consists of 2 n^+ -junction columns and 6 surrounding p^+ -ohmic columns [13]. Fig. 11 shows details of the sensor layout.

Pixel read-out electronics is based on the FE-I4 chips. The sensors are coupled to the chip with negative charge collection. Each readout channel contains an independent amplification stage with adjustable shaping, followed by a discriminator with an independently adjustable threshold. The chip operates with a 40 MHz externally supplied clock. The time over threshold (ToT) with 4-bit resolution together with the firing time are stored for a latency interval until a trigger decision is taken. The FE-I4 chip can also send a trigger signal via the HitOr line, which is formed as the logical OR of three fired discriminators on the FE-I4 chip [13].

3.1.3 The Time-of-Flight Detector

The way to distinguish signal from interactions of interest and pile-up is to measure the time of arriving protons using a high resolution ToF detector. To reject background at high luminosity, where the average number of interactions per crossing exceeds 50 ($\mu > 50$), the timing system should have the following characteristics [13]:

- resolution 10 ps or better,
- acceptance that fully covers the tracker,
- high efficiency ($> 90\%$),
- high rate capability of O(5) MHz per PMT pixel (and electronics channel),
- segmentation in x (horizontal) for multi-proton timing,
- Level 1 trigger capability,
- radiation hardness for $> 100\ \mathrm{fb}^{-1}$ run operation.

Due to the limited space of the Roman Pot, the ToF detector group was forced to use a modified version of the original Quartic detector. The Quartic detector detects the Cherenkov light caused by particles travel at nearly the speed of light to measure the arriving time. The original Quartic detector consisted of straight quartz bars positioned at the Cherenkov angle with respect to the proton flight direction, and functioning both as a radiator producing Cherenkov light, and as a light guide that funnels the light to the phototube. The logic is shown in the left picture of Fig. 12. The bars used by the AFP ToF have a new shape, the so-called ”LQbar”, as shown in the right picture of Fig. 12. It consists of an array of 4×4 quartz bars pointing to the Cherenkov angle ($48°$) in $x - z$ plane. The four layers of bars are labeled with number 1, 2, 3, 4 from top to bottom in the right picture of Fig. 12, a layer is called as a ”train”, the four bars in each layer are labeled with A, B, C, D from right to left in the right picture of Fig. 12. The bars in train 1 to train 4 have a width of 2 mm, 4 mm, 5 mm, 5.5 mm along the x direction, all of the bars are 6 mm wide along the z-axis, the coming protons will hit bar A firstly, then hit bar B, C, D. Since the bars are oriented at Cherenkov angle, the length of the bars decreases with increasing z such that the effective path length of the Cherenkov light to the PMT is independent of where the photon is emitted along the path of the proton. Train 1 is the narrowest one in the four trains because it is the closest to the beam center, so that the radiation at train 1 will be the heaviest and then to make the working time of the bars in this train not too different from others, their width have to be smaller to get less radiation. The Cherenkov light travels up the bars and is converted to a signal by a specialized 4×4-pixel Microchannel-Plate Photomultiplier (MCP-PMT) produced by Photonis.

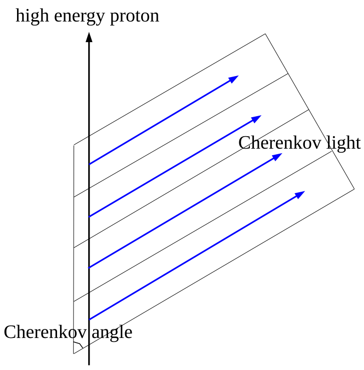

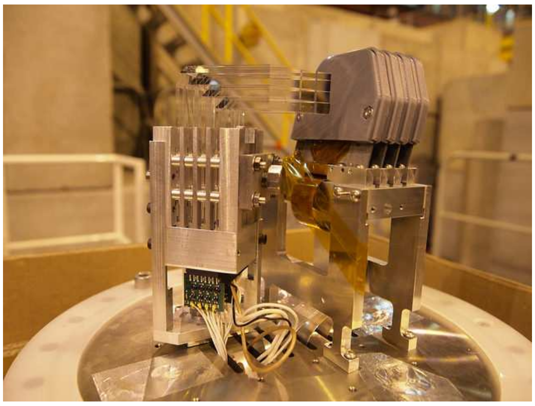

Figure 12. Detecting particles traveling at nearly the speed of light with quartz bars Cherenkov radiation (left). The Time-of-Flight detector (right).

3.2 The Forward Region and AFP Simulation

3.2.1 The Forward Region Simulation

Forward region simulation packages [14] allow full Geant4-based simulations of particles in the forward region. The simulation, digitization and reconstruction are implemented in the ATLAS data processing and analysis framework (Athena). Geant4 [15] is a toolkit for the simulation of the passage of particles through matter. A tracking process starts from the initial point of a particle, until the particle stopped by materials. Geant4 calculates the position, momentum and energy deposit at every step, the length of a step is based on the interaction it describes. The forward region simulation packages set up the geometry and magnetic field of the ATLAS forward region, including the geometry of beam pipe, magnets, collimators and the magnetic induction. Positions, rotate angles of the magnets and the width of collimators can be set through the simulation job option. The magnetic induction is calculated from K0L (dipole bending angle) and K1L (quadrupole strength·length) got from twiss files. The Geant4 output of every step can be stored in an ATLAS hits collection (Simulation Hit Collection), with the information in this collection, it is possible to visualize simulated hits in the forward region and perform detailed analysis. However, the size of a file with information of every step stored can easily reach several Gigabits, so this function is not switched on by default. It can be switched on via the simulation job option if visualization of hits in forward region or other detailed studies is needed.

3.2.2 The AFP simulation

The geometry of AFP is described by the AFP_GeoModel [16] package, an Athena package that constructs physics volumes of the RP, the SiT and the ToF. The physics volumes can be visualized through "Visualization Point 1" (VP1), which is a Geant4 function developed to a toolkit in Athena. The VP1 [17] drawings of these volumes in a simulation are shown in Fig. 13. The first two pictures show the physics volume of the Roman Pot, the other two pictures are visualization of the physics volumes of the Silicon Tracker. Simulation framework of the ToF detector is not finished yet. A fast Cherenkov model of

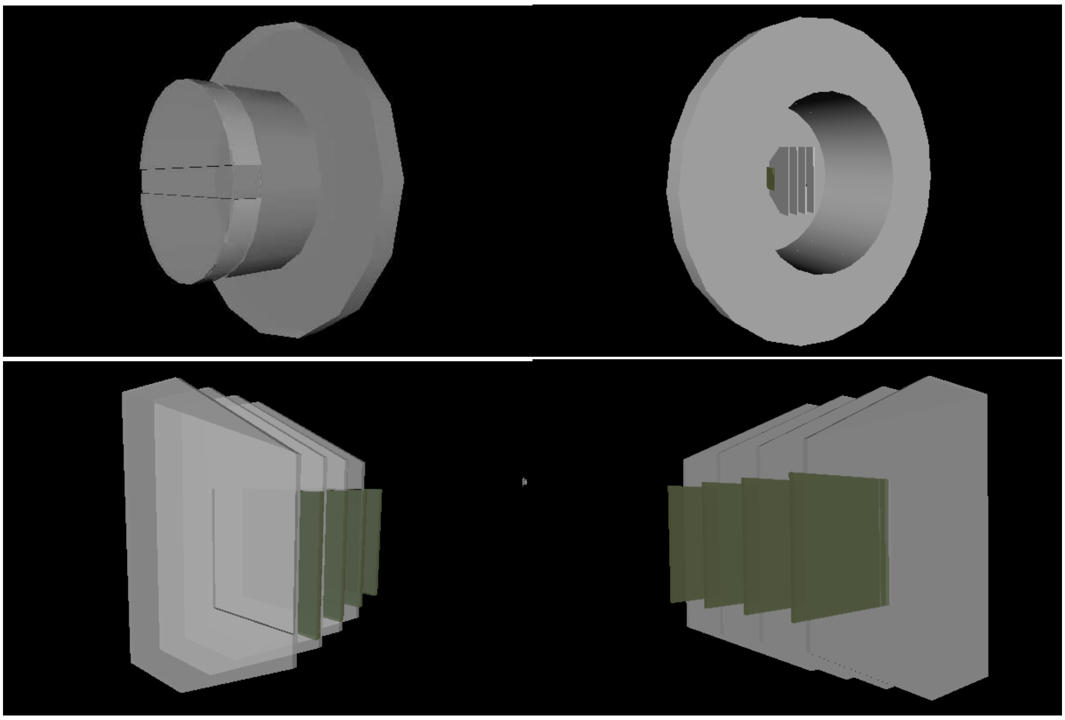

Figure 13. VP1 drawings of the Roman Pot and the silicon tracker.

the quartz bars was implemented because the simulation of optical processes is very time-consuming in Geant4. However, the ToF bars have a new construction making existing fast Cherenkov model mot valid any more.

The AFP data model mainly includes the collections of simulated hits in AFP sensitive detector volumes and the AFP hits containers, the AFP tracks containers in structure of Run2 ATLAS Object Data (xAOD). The simulated hits collections store informations about time, hit positions, kinetic energy, energy deposition, PDG ID, hit volume ID (station ID and layer ID) from Geant4 output straightly. Other parameters like pixel Row and pixel Col are calculated in the AFP sensitive detector algorithm.

The physics that AFP is interested in is represented by diffractive processes, so the positions of the AFP stations need to have high acceptance for diffractive protons and low acceptance for other processes like elastic scattering and non-diffractive processes. The acceptance of the AFP can be studied with the full simulation. The left plot in Fig. 14 shows the energy loss ξ - p_T distributions of all the out-coming protons in minimum bias (all of the soft QCD processes) samples generated by Pythia8. The acceptance plot on the right was got from the ratio of the number of out-coming protons with hits in the first sensor in the near station and the number of all the out-coming protons, ratio numbers were calculated in each bin to get this acceptance distribution with axises of energy loss ξ and p_T. The red region in the acceptance plot in Fig. 14 is dominated by single diffractive process. The regions below and above the high acceptance region are dominated by elastic scattering and non-diffractive processes. It is clear that the positions selected for AFP have very high acceptance for diffractive protons, very few of elastics scattered protons and non-diffractive protons can arrive at these positions. With the help of full simulation, it is also possible to study the shower development (see Sect. 4) and the radiation envi-

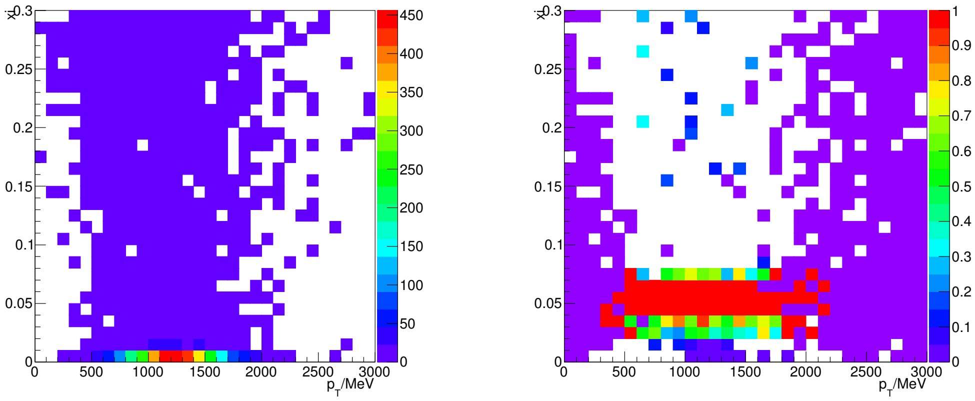

Figure 14. Distribution of all the protons in minimum bias samples with axises of Energy loss ξ - p_T (left); acceptance distribution got from the ratio of the number of events with hits in the first sensor in the near station and the number of all the events in each bin (right).

ronment at the AFP stations (see Sect. 5).

The AFP digitization algorithm was written within the general ATLAS scheme which includes the possibility to add pile-up events. At the digitization step, the information about hit station ID, layer ID, Row, Col and energy deposition is taken from the simulated hits collection and transform to the signal recorded by the detectors. It needs 3.6 eV to produce an electron-hole pair in the silicon sensor, so the energy deposition is converted to ADC with

$$\text{ADC} = \text{energy deposition}/3.6\ \text{eV}$$

Other parameters are passed from simulation to digitization directly.

3.2.3 The AFP track reconstruction

Individual signals recorded in detector channels are called hits, a physics analysis requires tracks which are reconstructed from the hits. The reconstruction algorithm uses the Kalman fit method [18]. This is the technique most of the tracking detectors use. It consists of the following steps:

a) calculation of a position of each pixel in the ATLAS coordinate system.

b) selection of the hits with cut $\text{ADC} > 1500$ (ADC is the number of electron hole pair in a pixel) in the first and the second sensors of each station, if there are hits close to each other along the x-axis, the position of this cluster is calculated as the weighted average:

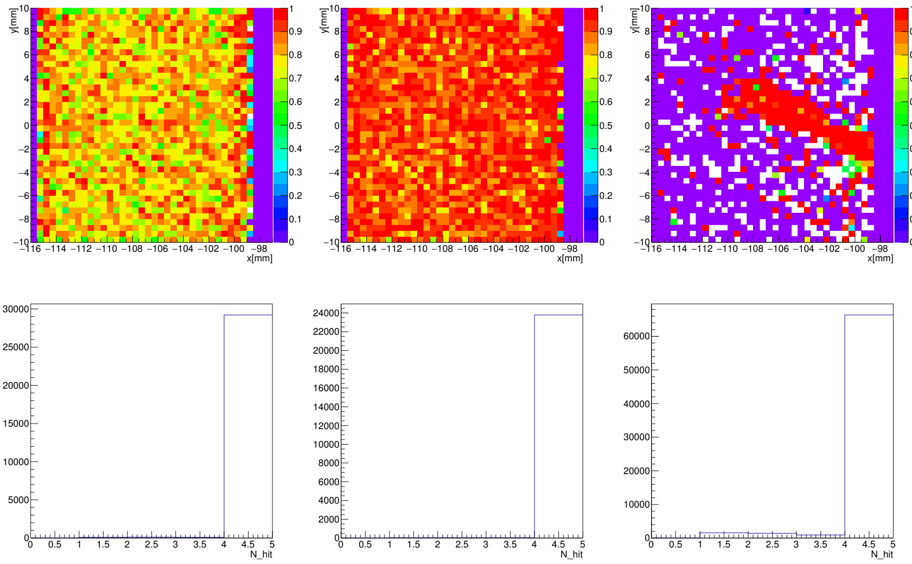

Figure 15. The upper plots are track reconstruction efficiency of protons with slope in [0, 0.01] generated by particle gun just in front of the AFP near station (left), protons with slope in [0, 0.001] generated by particle gun just in front of the AFP near station (middle), single diffractive events generated by Pythia8 (right). The bottom plots are the number of hit layers in the events with hits in the first plane. 98.85 %, 99.46 %, 94.50 % protons have hits in four planes in the slope 0.01 samples, slope 0.001 samples, single diffracitve samples.

$$\overline{x} = \frac{\sum_i x_i \times \mathrm{ADC}_i}{\sum_i \mathrm{ADC}_i}$$

The ADC value of this cluster will be summed over the pixels included.

c) cluster in the first sensor and a cluster in the second sensor is combined to a track candidate, called "track seed". All combinations are considered. A cluster here means a single hit if the hit is isolated from other hits or a group of hits close to each other along the x-axis.

d) selection of hits with $\mathrm{ADC} > 1500$ in the remaining layers, then fit the hits in each layer with the track seed using Kalman fit method. If the hits in the third layer can fit with a track seed with a result of $\chi^2 < 2$, these hits and the track seed are reconstructed as a track.

e) if the hits in the fourth layer can fit with a track seed with a result of $\chi^2 < 2$, no matter if the hits in the third layer in this event can fit with the track seed, a track is reconstructed.

At the step b), the position of a cluster is calculated from the average position of hit pixels close to each other along the x-axis weighted by energy deposition, the pixels close to each other along the y-axis are not taken into account because the pixel size on y is 0.25 mm and there is no rotation around the x-axis, it is very rare for a proton to hit two pixels close to each other along the y-axis at the same time.

From the simulation result, a proton not accompanied by showers usually hit two pixels close to each other along the x-axis, such clean events are the samples that physics analyses are interested in, so that considering only pixels close to each other along the x-axis is enough.

The track reconstruction method is able to reconstruct the diffractive proton tracks with high efficiency. To check this, we studied the track reconstruction efficiency in the near station in simulation. The efficiency was calculated from the ratio of the number of events with tracks in the near station and the number of events with hits in the first sensor in the near station. Fig. 15 shows the track reconstruction efficiency of protons generated by particle gun and single diffractive events generated by Pythia8. The reconstruction efficiency of single diffractive proton tracks is very high, but it becomes lower when the slope of particles becomes larger. The reason is clear: the cut $\chi^2 < 2$ was designed for small slope tracks reconstruction, so this method does not have very high efficiency on large slope track reconstruction as tracks with large slope can not be diffractive proton tracks.

3.3 The AFP Trigger System

The AFP first-level trigger in 2016 runs was based on the HitOR signals from FE-I4 chips. The HitOR tracking trigger cannot be used for pile-up rejection. The AFP High-Level Trigger (HLT) strategy will depend on the detector configuration, the instantaneous luminosity and the physical process to be measured. The main triggers used in the presented analysis are listed below. Note that L1 triggers instead of HLT triggers were used because most of the HLT triggers were prescaled heavily and some of the HLT trigger were not active in data processing.

- L1_AFP_C_AND: both the near and the far stations on C side triggered.
- L1_AFP_C_MBTS_A: both the near and the far station on C side and the Minimum Bias Trigger Scintillator (MBTS) [20] on A side fired.
- L1_AFP_FSC: AFP far station on C side triggered.
- L1_AFP_C_ANY: AFP near station or the far station on C side triggered.
- L1_AFP_C_ANY_UNPAIRED_ISO: the near station or the far station on C side triggered but the bunch is unpaired.

The MBTS in Run 1 consisted of 16 counters per side, of which 8 form an inner ring and another 8 an outer ring covering in total a pseudo-rapidity range of $2.1 < |\eta| < 3.8$ in the forward direction of each beam. They are mounted at $|z| = 3.6$ m between the Inner Detector and the Liquid-Argon-Calorimeter. In the Run 2 upgrade, the 16×2 channels were replaced to 12×2 channels, the outer rings have 4 channels and the inner ring have 8 channels. The upgrade also changed MBTS geometry slightly to increase η coverage.

The bunch information in trigger L1_AFP_C_ANY_UNPAIRED_ISO is from the Beam

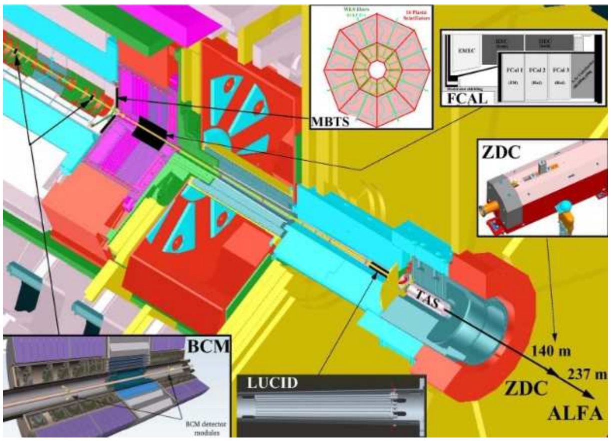

Figure 16. MBTS and BCM in the ATLAS detector. [21]

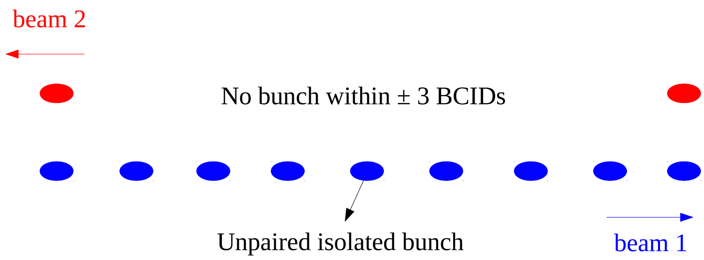

Figure 17. An unpaired isolated bunch.

Conditions Monitor (BCM) [19]. It consists of two detector stations (forward and backward) with four modules each. A module consists of two polycrystalline chemical-vapour-deposition (pCVD) diamond sensors, glued together back-to-back and read out in parallel. The modules are positioned at $z = \pm 184$ cm.
In the LHC runs in Run 2, the Radio-Frequency was operated at a frequency of 400 MHz. This corresponds to buckets every 2.5 ns, groups of ten buckets are assigned the same Bunch Crossing IDentifier (BCID). The bunch space in Run 2 is 25 ns, each bunch corresponds to a specific BCID. In colliding beam, both beam 1 and beam 2 are filled with bunches, such situation is called as paired bunches. It is possible that a bunch does not have its paired bunch in the other beam, if a bunch in only one LHC beam with no bunch in the other beam within ± 3 BCIDs, it is an unpaired isolated bunch.

4 Shower Development and Beam Induced Backgrounds

When a high energy proton interacts with a material, a particle shower might be created and affects the AFP detectors. The showers can be caused by the beam pipe, the AFP stations and the collimators, the silicon sensors themselves are also possible source of showers.
There are several sources of beam induced background: IP secondary interactions, interaction with the AFP stations, backscattering due to collimators after the AFP, part of the beam gas interactions (a proton interaction with residual gases can produce showers but

also can be just scattered).
It is difficult to distinguish diffractive protons and beam induced background if the sample contains a lot of showers, so an effective way to remove showers is needed. In this background estimation analysis, only tracks passing the shower removal selection were considered. The processes with interest are diffractive scattering, other processes detected by the AFP detector are treated as backgrounds, including beam induced background and non-diffractive background. The non-diffractive background can be studied via simulations.
The beam induced background, after removing showers, is considered as originating due to beam halo and scattered protons produced in beam gas interactions. Such background occurs randomly and it is hard to simulate, but can be estimated from data. As will be shown, the beam halo is the most significant component of background in the AFP detector.

4.1 Shower Development

It is possible to study the showers caused by the materials near the AFP detectors with particle Gun (pGun) generator, a generator which able to shoot particles with given position, momentum and particle type (PDG ID).
If protons are produced just in front of the AFP station and shoot straightly to the tracker, then all of the showers should be caused by materials in the AFP station and beam pipe near the station. By comparing the shower development in different Monte Carlo samples, we found the amount of showers are correlated to the slope of protons.
Below is a comparison of the number of hits in each layer got from protons with slope in [0,0.01] generated by particle Gun just in front of the AFP near station, protons with slope in [0,0.001] generated by particle Gun just in front of the AFP near station, single diffractive process generated by Pythia8. The values are all normalized to the number of hits in the first sensor in the near station in each kind of sample. Numbers are arranged in this order: first layer in the near station→second layer in the near station→third layer in the near station→forth layer in the near station→first layer in the far station→second layer in the far station→third layer in the far station→forth layer in the far station.

pGun samples with slope of protons in [0,0.01]:
1→1.1194→1.2092→1.3940→8.6708→9.5387→9.7361→9.8371.
pGun samples with slope of protons in [0,0.001]:
1→1.1259→1.1974→1.3674→5.2172→5.6792→5.8332→5.9415.
Single diffractive samples:
1→1.3496→1.9892→3.0773→3.8571→4.6176→4.2448→5.2577.
Run 305359 data:
1→1.0911→1.3137→no sensor→1.9462→4.0523→4.6592→6.1408.

Many showers occurred between the last sensor in the near station and the first sensor in the far station in the samples generated by particle Gun. Over 90 % of the shower particles are electrons. Based on the distributions of reconstructed x' - truth level p_x got from the three kinds of samples in Fig. 18, it is clear that the amount of showers raises

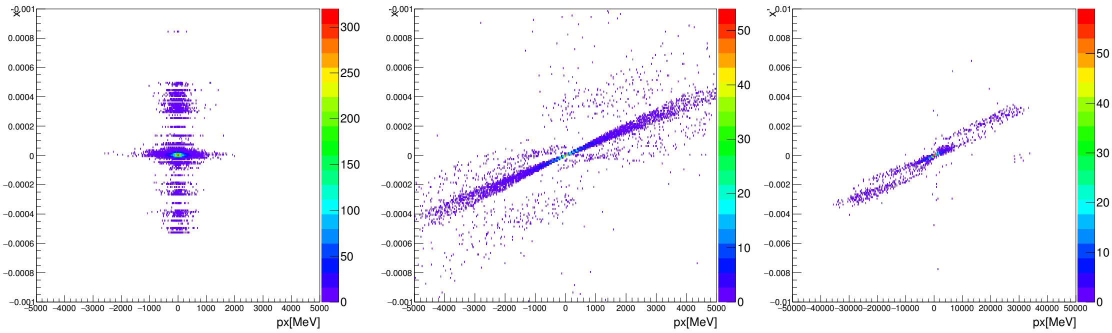

Figure 18. Reconstructed x'-truth level p_x distributions for single diffractive samples (left), pGun samples with slope in [0, 0.001] (middle), pGun samples with slope in [0, 0.01] (right).

fast with the slope of protons.

If a proton did not cause showers, it usually causes two or three hit pixels per sensor in both the near station and the far station, as shown in Fig. 19. Most of the protons generated by pGun did not arrive at the far station due to their slope is too large, but they caused much more electron showers upstream to the far station than the single diffractive protons. We studied the starting points of the showers with visualization of hits in the forward region and verbose tracking output of an event with many showers got from simulation. Fig. 20 shows the VP1 drawings of the hits in an event contains a proton generated by particle gun just in front of the AFP near station, the slope of this proton was 0.01 and it caused many shower electrons. The IP1 is at the right side of these plots, the blue points are simulated hits, the lines with different colours are tracks formed by the hits. Each kind of particle has a specific colour. Most of the tracks in this event are pink, which means they are electrons.

The four clusters (see Fig. 20 a) are caused by shower electrons interacting with the forward detector envelope (ForDetEnvelope), a physics volume filled with air in simulation. The initial purpose of this ForDetEnvelope was to model the material out of the beam pipe, but the material of forward region was changed to be defined in the forward region geometry package, this package sets not only the region inside the beam pipe but also the region out of the beam pipe to vacuum. Only the gaps cut for the AFP detectors and the ALFA detectors were still filled with the material defined in forward detector envelope package. The starting points of the showers are at about 3.5 m after the generated place of the proton, this position does not depend on the generated place of the proton because the tube has a radius of 40 mm, a proton with slope of 0.01 will hit the tube after travelling about 4000 mm and it will cause electron showers when it hits the tube. The shower electrons will go all directions, but the hits can only be recorded by Simulation Hit Collection (see Sect. 3.2.1) when the electrons hit volumes, so the shapes of the four clusters are limited by the range of ForDetEnvelope, as shown in Fig. 21.

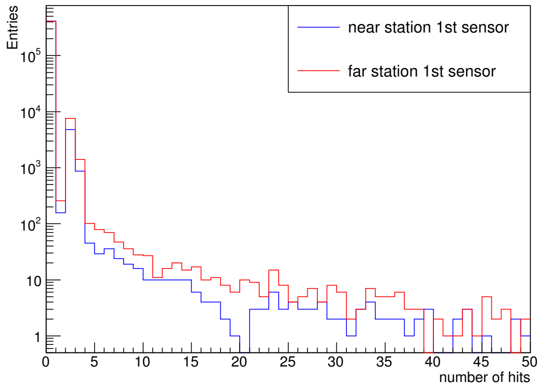

Figure 19. Hit multiplicity of the first sensor in the near station and the far station.

4.2 Removal of Showers

Based on the study of showers in Sect. 4.1, we found several signatures which can be used to identify them:

a) protons which can cause showers usually have slope larger than 10^{-3},

b) if a proton is accompanied by a shower which originated before it hits the AFP SiT, the number of reconstructed tracks in the near station is usually more than two, the number of hits in the first sensor in the near station is usually more than three,

c) reconstruction of shower tracks is usually not as well as of high energy proton tracks because of the large slope.

As described in Sect. 3.2, the track reconstruction method requires hits in the first sensor and hits in the second sensor, then fit the track seeds with hits in the remaining sensors, if a particle hits the first sensor and causes shower particles after the hit, then the shower particles do not leave hits on the first sensor. So the track reconstruction will not reconstruct shower tracks started after protons hitting the first sensor in the near station. However, the near station and the far station are treated separately, so the showers originated in the near station has the possibility to be reconstructed in the far station. A method to remove such showers is to match the tracks in the far station with the tracks in the near station. The easiest way is to select events with one track reconstructed in the near station and one track reconstructed in the far station. The events with exactly one track, they are called as "golden events". Shower tracks originated before protons hitting the AFP stations could also be reconstructed, several ways can be used to remove such showers, e.g. cuts on number of hits, cuts on number of tracks. The relatively best way is to use a variable called "track quality". defined as:

$$\mathrm{Trk\_quality} = \mathrm{N_{planes}} + \frac{\chi^2_{\mathrm{max}} - \chi^2_{\mathrm{trk}}}{\chi^2_{\mathrm{max}} + 1}$$

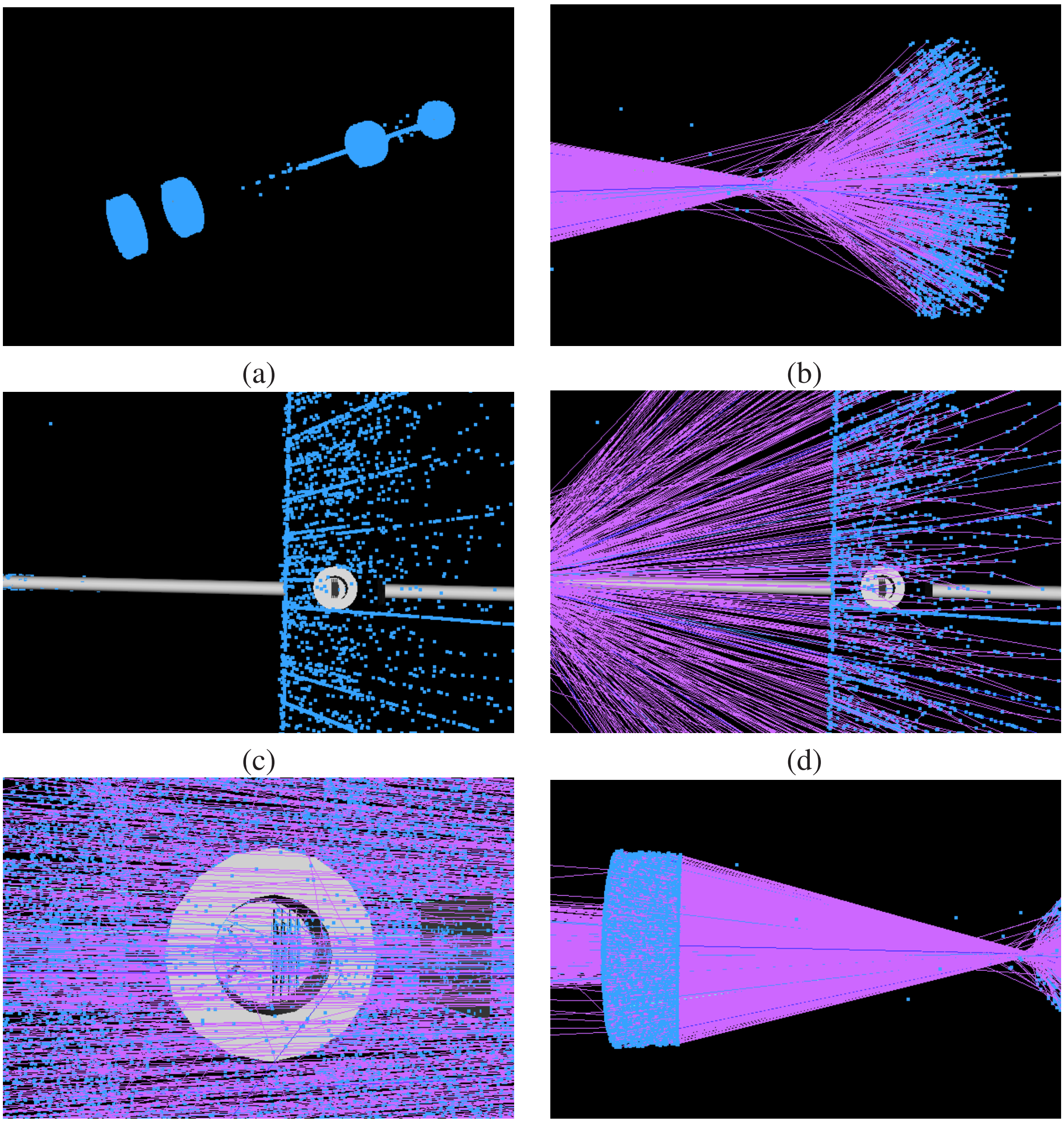

(a) (b) (c) (d) (e) (f)

Figure 20. Hits in an event generated by pGun, the generated position of the proton was at (x = -105.0 mm, y = 0 mm, z = -205100.0 mm), the x-slope was -0.01. IP1 is at the right side of the pictures. (a) The view from position very far from the IP on C side. (b) The starting points of the electron showers is at about 3.5 m after the generated point of the proton. (c) The showers at the AFP near station and the beam pipe. (d) The showers started at z = -208.5 m upstream to the AFP near station. (e) The showers at the AFP far station. (f) The showers started at z = -208.5 m downstream to the AFP far station.

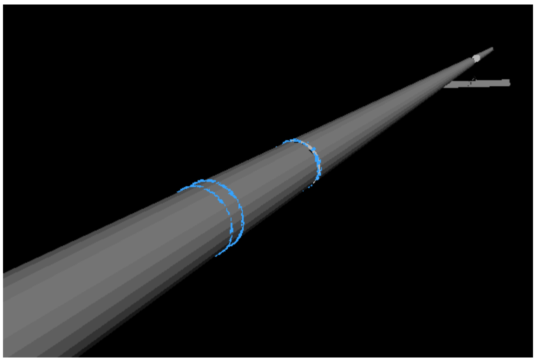

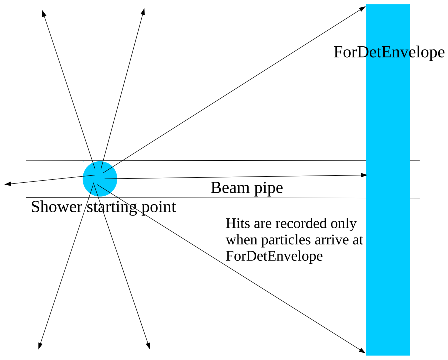

Figure 21. The clusters are limited by the range of ForDetEnvelope, the tube in the left picture is the mother volume defined in forward region geometry package.

where $\mathrm{N_{planes}}$ is the number of hit planes used in the reconstruction. χ^2_{trk} is the Kalman fit result of a reconstructed track. χ^2_{max} is the cut value used on cutting χ^2_{trk} in reconstruction, the better the fitting was, the smaller χ^2_{trk} we got. Initially the cut used on Monte Carlo reconstruction was $\chi^2_{\mathrm{max}} = 2$, but the inter-plane alignment in 2016 data was not good enough so the cut was changed to $\chi^2_{\mathrm{max}} = 3$, to accept more tracks. Trk_quality increases with the decrease of χ^2_{trk}. So a better reconstructed track has larger track quality.
Based on these signatures a method to remove showers was developed. It has the following steps:

1. Selection of the tracks passing cut $\mathrm{Trk\_quality} > 3$ in the near station, passing cut $\mathrm{Trk\_quality} > 4$ in the far station in an event (in the configuration in 2016, the near station had three plates, the far station had four plates).

2. Loop over the selected tracks in the near station; each track in the near station is combined with all the selected tracks in the far station to form clean track seed.

   (a) Selection of the clean track seed with cut: $\sqrt{(x_{far} - x_{near})^2 + (y_{far} - y_{near})^2} < 2.4\ \mathrm{mm}$, $|x'_{far} - x'_{near}| < 0.002$.

   (b) For each track in the near station, if there are tracks in the far station can pass the cut, select the one with the smallest value of $|(x_{far} - x_{near}) - x'_{near} \times 12000\ \mathrm{mm}|$. Every track can be used no more than one time, if a near station track match with a used far station track the best, they will not be selected as clean tracks.

The basic requirements for this shower removal method are: it can remove showers effectively and most of single diffractive events should be able to pass the selection. This method was tested on single diffractive Monte Carlo samples, the ForDetEnvelope was filled with air and the AFP stations were 1.5 mm from the beam center in this Monte Carlo production. Over 90 % of the events have at least one track in the near station passing the selection. The ratio can be affected by the cuts at the third step. More tracks will pass the selection if less tight cuts are used, but the ability of rejecting showers will become

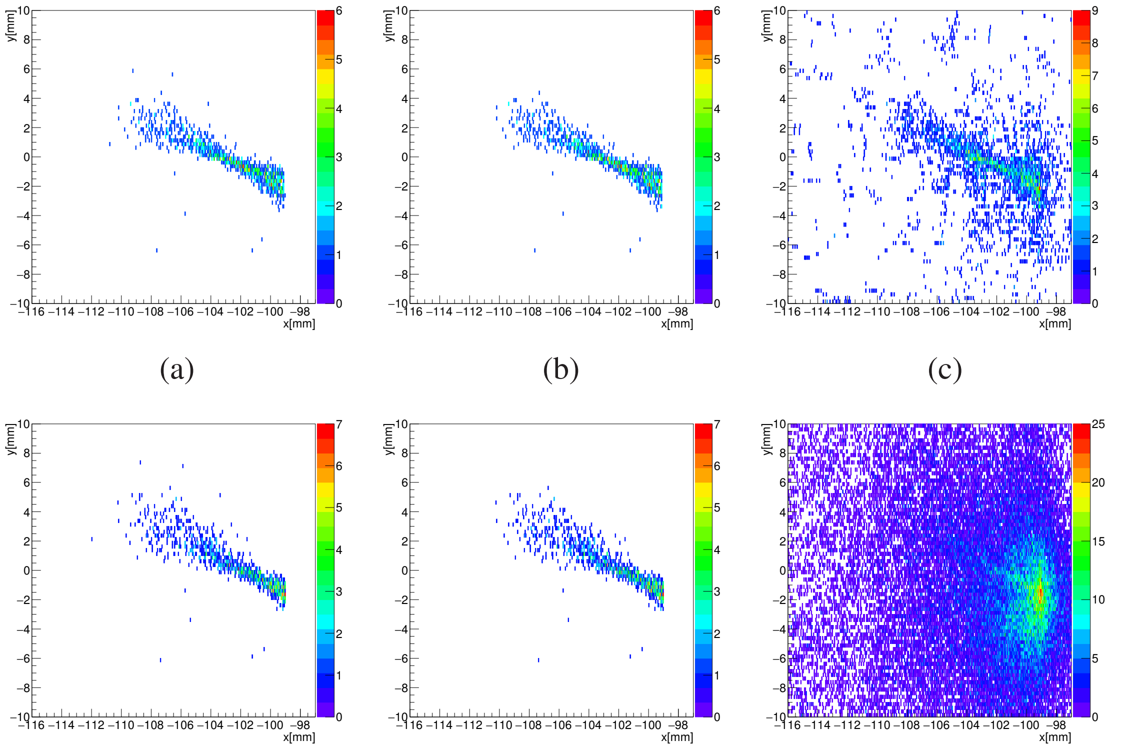

(a) (b) (c)

(d) (e) (f)

Figure 22. Track maps for single diffractive Monte Carlo samples. The AFP stations were 1.5 mm from the beam center. (a) Track map of the near station for golden events. (b) Track map of the near station after applying shower removal selection. (c) Track map of the near station without any cut. (d) Track map of the far station for golden events. (e) Track map of the far station after applying shower removal selection. (d) Track map of the far station without any cut.

weaker. The cuts used here are tight enough to reject nearly all of the showers and it can let most of the single diffractive events pass. Fig. 22 shows the track maps for these single diffractive Monte Carlo samples before and after removing showers. This method works well on simulation as the sensors in simulation are aligned ideally. Unfortunately, the estimation of beam induced backgrounds was based on Run 305359 data, the reconstruction of Run 305359 data did not have a good enough inter-plane alignment result, so the slope information is not reliable yet. As such, the slope cut was not applied at the third step and the slope information was not used in the calculation at the forth step when selected clean tracks in data. The slope information was also not used on plotting the Monte Carlo distributions shown in Sect. 4.3 because the selection used on data and Monte Carlo should be kept the same when make data, Monte Carlo comparison.

4.3 Beam Induced Backgrounds

Several sources of beam induced background are caused by showers, such backgrounds should be removed after applying the shower removal selection. The remaining sources of beam induced backgrounds are high energy particles caused by beam halo and beam gas not accompanied by showers. Beam gas in this case should be protons scattered by the residual gas inside the beam pipe. It is hard to distinguish this kind of beam gas and beam halo, but from the results which will be shown, beam gas was not observed in Run 305359 data, the main process of beam induced backgrounds in the samples after removing showers is beam halo.

As described in Sect. 3.3, the bunches in events passing trigger L1_AFP_C_ANY_UNPAIRED_ISO are unpaired isolated, so the hits in AFP left by these events are caused by beam halo. One way to get a pure beam halo sample is to select the events passing this trigger in data, as shown in Fig. 23. The track maps and the track y position distributions are got from the unpaired isolated events after applying shower removal selection or golden unpaired isolated events in Run 305359 data. Based on the bin with the highest entries, the peak of track y-position distribution in the near station is at about -2.8 mm, the peak of track y-position distribution in the far station is at about -2.3 mm. It agrees with the y-positions of beam center at the near station and the far station considering that there was no well alignment in Run 305359 data. A data driven method could be used to describe the beam halo distributions in colliding bunches. The logic of this data-driven method is to use the beam halo in these unpaired isolated bunches as the model to fit beam halo in colliding bunches. The beam halo hits in colliding bunches might be a little different from the beam halo hits in unpaired bunches due to the interactions between bunches, such difference was not observed in this study, so it can be ignored.

The physics processes which have the possibility to be detected by the AFP detectors can be studied via simulations. These processes include single diffraction, central diffraction, elastic scattering and non-diffraction. Pythia8 was used as the generator of these processes. Single diffraction and central diffraction are signal processes of the AFP detector, cross section of single diffraction is ten times of cross section of central diffraction. Non-diffraction and elastic scattering are considered as physics background. Cross sections of the physics background processes are much bigger than that of the diffractive processes, but based on the study of AFP acceptance in Sect. 3.2.2, the AFP sensors have very low acceptance for non-diffractive protons and elastics scattered protons, so the tracks measured by the AFP after removing showers are still dominated by single diffractive protons. As shown in Fig. 24 and Fig. 25, the first one shows track maps and track y-position distributions for single diffractive Monte Carlo samples, the second one shows the same distributions for minimum bias Monte Carlo samples, the shower removal selection and the golden events selection were applied to both kinds of samples. Minimum bias samples include all the soft QCD processes (single diffraction, central diffraction, elastic scattering, non-diffraction). Positions of the detectors were the same as the configuration in 2016 in these Monte Carlo productions. The distributions of these two kinds of Monte Carlo samples are slightly different, such difference comes from the non-diffractive protons and elastics scattered protons.

In this study, the physics background was included in simulation and it was not estimated. In both kinds of samples, the region with hits in the near station is dominated in $-1\,\mathrm{mm} < y < 5\,\mathrm{mm}$, the region with hits in the far station is dominated in $-0.4\,\mathrm{mm} < y < 6.4\,\mathrm{mm}$, this signature provides a way to cut off these physics processes: $y < -1.5\,\mathrm{mm}$ in the near station and $y < -1.0\,\mathrm{mm}$ in the far station. We moved

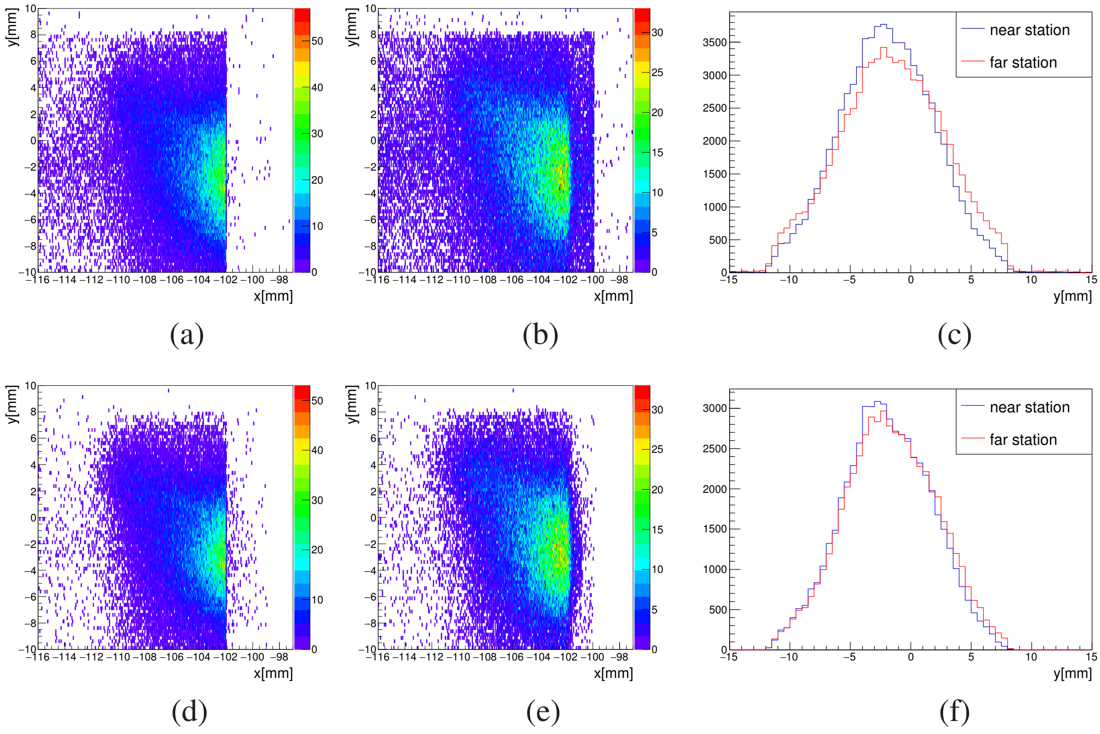

Figure 23. Track maps and track y-position distributions for unpaired isolated events after removing showers in Run 305359 data. For golden events: (a) Track map in the near station. (b) Track map in the far station. (c) Track y-position distribution in the near station and the far station. For events passing the shower removal selection: (d) Track map in the near station. (e) Track map in the far station. (f) Track y-position distribution in the near station and the far station.

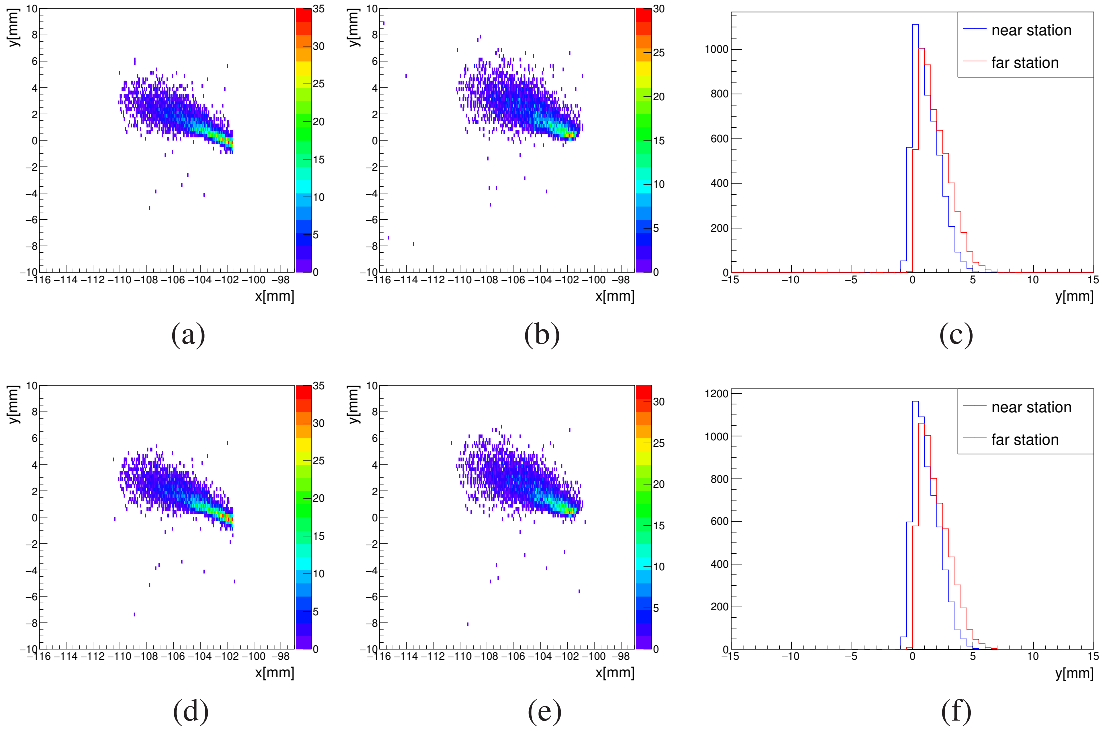

Figure 24. Track maps and track y-position distributions for single diffractive Monte Carlo golden events and events after removing showers. The AFP stations were at the position as in Run 305359. For golden events: (a) Track map in the near station. (b) Track map in the far station. (c) Track y-position distribution in the near station and the far station. For events passing the shower removal selection: (d) Track map in the near station. (e) Track map in the far station. (f) Track y-position distribution in the near station and the far station.

the cut values 0.5 mm smaller because data did not agree with simulation very well, some tracks from physics processes would also be able to pass the cuts if the cuts developed in simulation were moved to data without any changes.

The single diffractive process has one proton remain intact and the other one dissociate into a multi-particle state, so the MBTS detector on the opposite side of the side where a proton was detected by the AFP detector could be fired by a single diffractive process. It indicates a way to tag single diffractive events in data: MBTS inner modules without signal on the side where a proton was detected by the AFP detector, MBTS inner modules with signal on the other side. The logic is shown in Fig. 26. This requirement can be translated to trigger cuts, L1_AFP_C_AND and L1_AFP_C_MBTS_A be fired at the same time. The first trigger means the event has signals in both the near station and the far station on C side, the second trigger means the MBTS trigger on A side was fired in this event. Trigger L1_AFP_C_AND requires the proton remained intect on C side, so the proton on A side was the one that dissociated into a multi-particle state and as such, these particles fired the MBTS trigger on A side. By requiring events passing L1_AFP_C_AND and L1_AFP_C_MBTS_A at the same time, we can select part of the single diffractive events in data, not all the single diffractive events can be selected in this way due to the

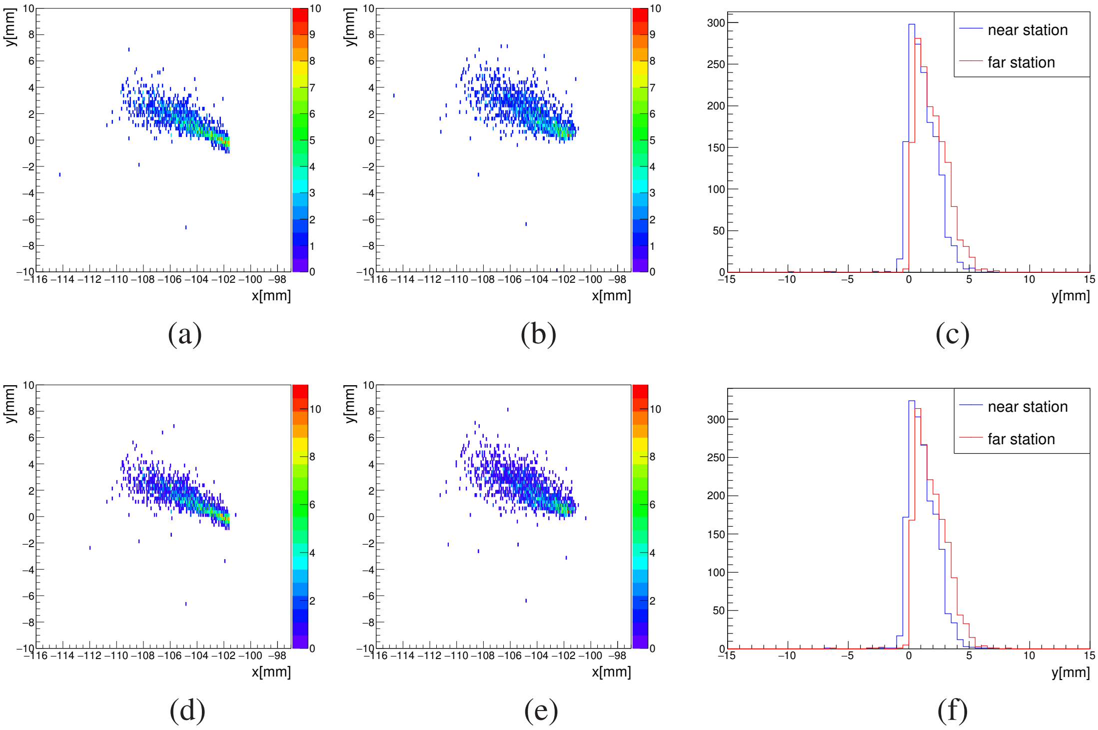

Figure 25. Track maps and track y-position distributions for minimum bias Monte Carlo golden events and events after removing showers. The AFP stations were at the position as in Run 305359. For golden events: (a) Track map in the near station. (b) Track map in the far station. (c) Track y-position distribution in the near station and the far station. For events passing the shower removal selection: (d) Track map in the near station. (e) Track map in the far station. (f) Track y-position distribution in the near station and the far station.

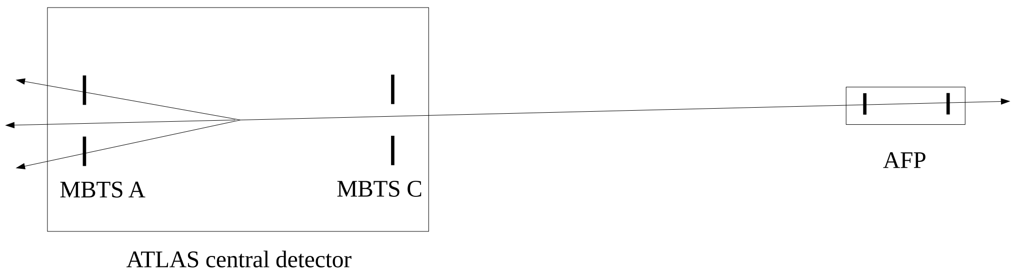

Figure 26. A single diffractive event fired L1_AFP_C_AND and L1_AFP_C_MBTS_A at the same time.

limited acceptance of MBTS. The track maps for these selected single diffractive events are shown in Fig. 27 (a), (b). The shapes of the distributions agree not bad with the single diffractive Monte Carlo.

This trigger cut is able to select single diffractive events. However, it can not veto on MBTS inner modules on C side. Another selection is to use MBTS hits, the selection was MBTS inner modules on A side have hits with charge (energy) larger than 0.15, MBTS inner modules on C side do not have hits with charge larger than 0.15. The energy threshold used in the selection was 0.15 % based on experience from the ALFA detector. Fig. 27 (c), (d) show the track maps for events passing this selection. Less events can pass the MBTS hits selection compared to the number of events passing the MBTS trigger selection but the MBTS hits selection selected a purer single diffraction sample. In the track maps, there are a few tracks in the region below the "red region", the fraction of these tracks in events selected by MBTS hits selection is smaller than events selected by MBTS trigger selection. From the track maps for single diffractive Monte Carlo samples and minimum bias Monte Carlo samples in Fig. 24 and Fig. 25, the physics processes do not have tracks in this region, so these tracks are probably beam induced backgrounds. The cut on number of MBTS inner module hits on C side was 0, it is the tightest cut but only 13.8 % tracks can pass the selection, which means some single diffractive proton tracks can not pass. To let more events pass the cut we can require number of MBTS inner module hits on C side smaller than a positive integer. There are 8 MBTS inner modules, so the cut value can be any integer between 0 and 8. Fig. 28 shows the track x-position distributions and y-position distributions for selected single diffractive events. The efficiency for cut $\mathrm{N_{MBTS\,C}} < 2$ is 39.8 %, for cut $\mathrm{N_{MBTS\,C}} < 4$ is 62.4 %, for cut $\mathrm{N_{MBTS\,C}} < 6$ is 78.4 %, for cut $\mathrm{N_{MBTS\,C}} < 8$ is 92.8 %.

The estimation of beam induced backgrounds level was based on data taken in the first AFP physics run: Run 305359. The selections for removing showers were applied to the data. Also, a cut requiring events not passing L1_AFP_C_ANY_UNPAIRED_ISO was applied because the tracks in the AFP left by these events are known to be beam halo and the unpaired isolated events were used as the model to fit the remaining beam halo events. From the track maps and track y-position distributions shown in Fig. 29, the region below the high density region has some tracks that single diffractive and minimum bias Monte Carlo do not have. Single diffractive events in data selected by the MBTS trigger selection or the MBTS hits selection have very few such tracks. The position of this part that did not appear in the single diffractive Monte Carlo samples or minimum bias Monte Carlo samples have similar signatures as the unpaired isolated events. The peak of the beam halo like events y-position distribution in the near station is at about y = -3.0 mm, in the far station is at about y = -2.6 mm, they agree with the positions of the beam center. Based on these signatures, we can conclude that the tracks in this region were caused by beam halo. The beam halo tracks and the diffractive proton tracks can be distinguished clearly from the distributions of track y-position. The beam halo parts have similar shape as the track y-position distributions of unpaired isolated events. The diffractive signal parts mixed with a few non-diffractive backgrounds are simulated by minimum bias Monte Carlo, so the data distributions respect the following fitting model

$$\mathrm{n_{data}}(y) = \mathrm{N_{minbias}} \cdot \mathrm{f_{minbias}}(y) + \mathrm{N_{background}} \cdot \mathrm{f_{background}}(y) \tag{24}$$

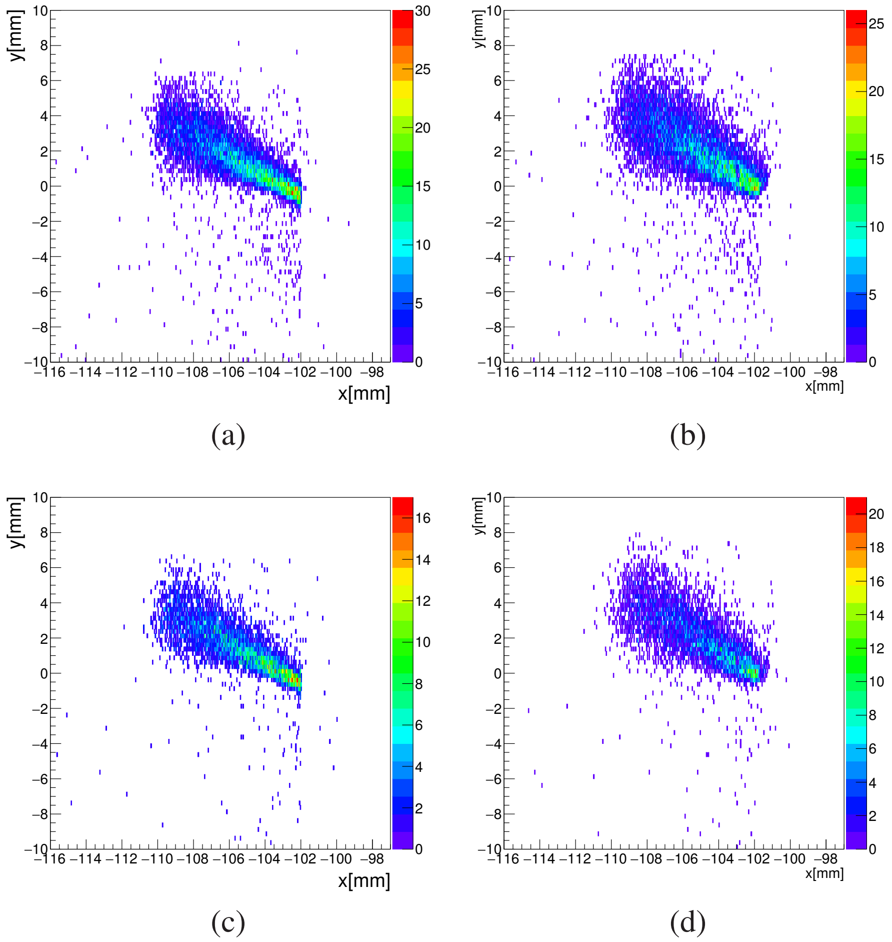

Figure 27. Track maps for selected single diffractive events after applying the shower removal selection. (a) Track map for events passing L1_AFP_C_AND and L1_AFP_C_MBTS_A at the same time in the near station. (b) Track map for events passing L1_AFP_C_AND and L1_AFP_C_MBTS_A at the same time in the far station. (c) Track map for events with MBTS inner modules hits on A side, without MBTS inner modules hits on C side in the near station. (d) Track map for selected events with MBTS inner modules hits on A side, without MBTS inner modules hits on C side in the far station.

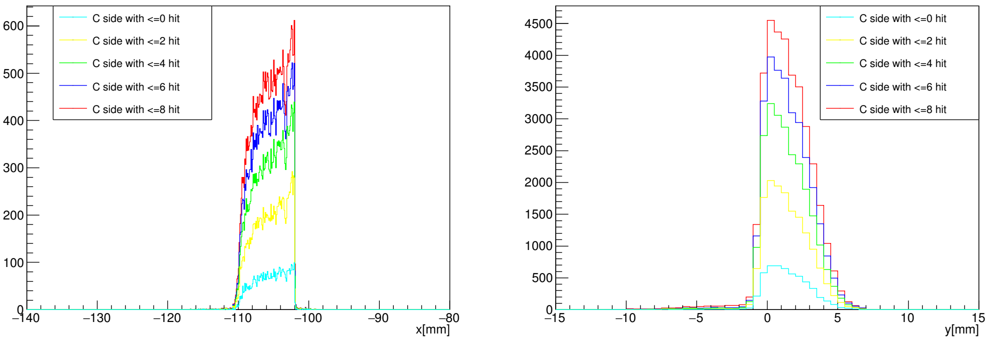

Figure 28. Track x-position, y-position distributions for selected single diffractive events with different cuts on MBTS.

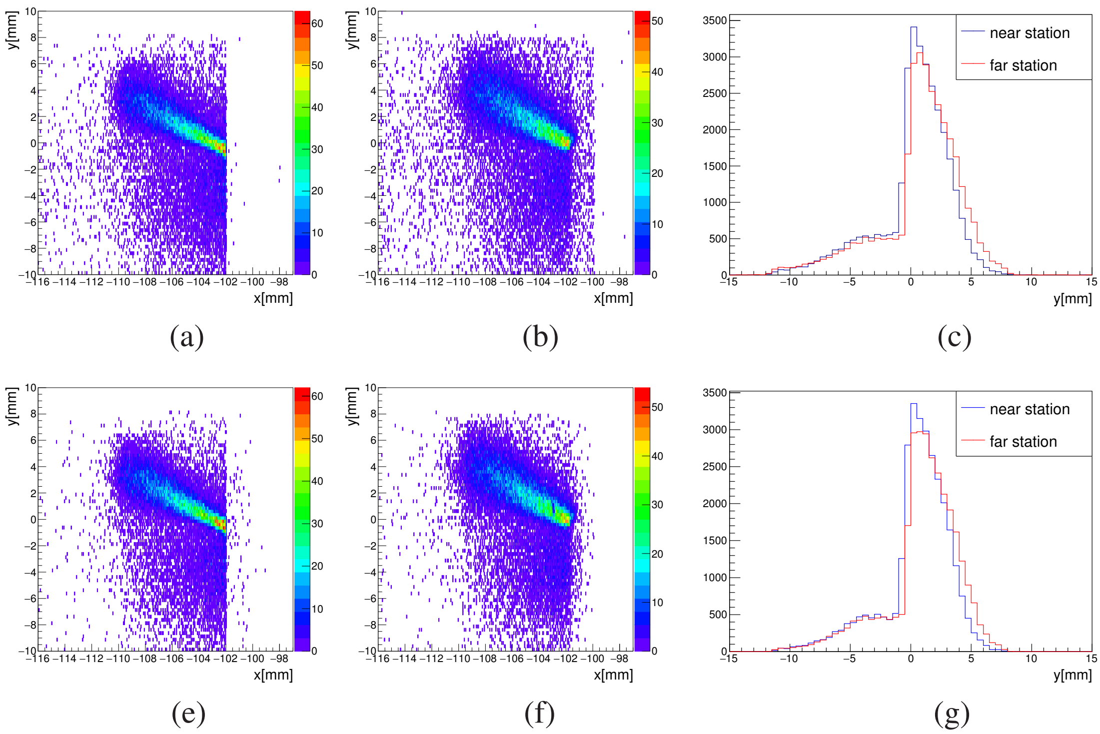

Figure 29. Track maps and track y-position distributions for paired bunch events in Run 305359 data after removing showers. For golden events: (a) Track map in the near station. (b) Track map in the far station. (c) Track y-position distribution in the near station and the far station. For events passing the shower removal selection: (d) Track map in the near station. (e) Track map in the far station. (f) Track y-position distribution in the near station and the far station.

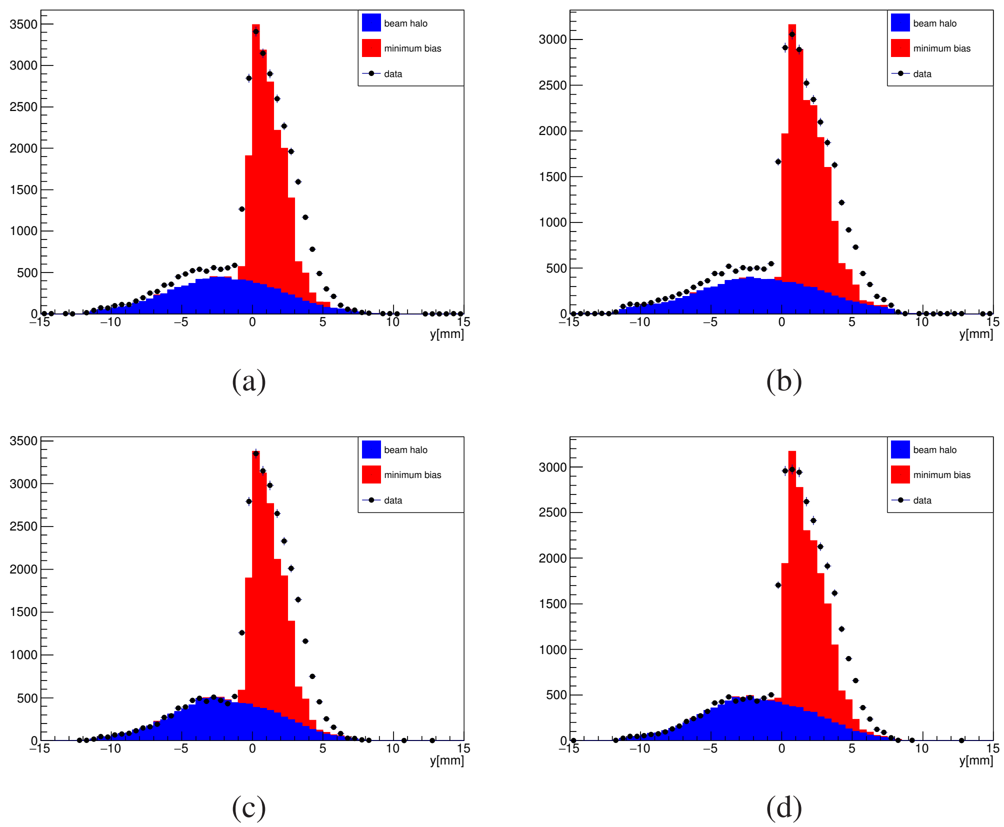

Figure 30. Models to describe beam halo. The red part is minimum bias Monte Carlo events, the blue part is unpaired isolated events after scaling, the black points are data events. (a) Track y-position distribution in the near station in golden events samples. (b) Track y-position distribution in the far station in golden events samples. (c) Track y-position distribution in the near station in shower removal samples. (d) Track y-position distribution in the far station in shower removal samples.

where $\mathrm{n_{data}}(y)$ is the y-position distribution of data events, $\mathrm{N_{minbias}}$ is the number of single diffractive events and non diffractive events in the model, $\mathrm{f_{minbias}}(y)$ is the possible density function (p.d.f.) got from the y-position distribution of minimum bias Monte Carlo. $\mathrm{N_{background}}$ is the number of beam halo events in the model, $\mathrm{f_{background}}(y)$ is the beam halo p.d.f. got from the y-position distribution of unpaired isolated events in Run 305359. From the y-position distributions for single diffractive and minimum bias Monte Carlo samples in Fig. 24 and Fig. 25, very few of the protons from soft QCD processes arrive at regions where $y < -1\,\mathrm{mm}$ in the near station and $y < -0.5\,\mathrm{mm}$ in the far station. This signature provides a beam halo control region by requiring $y < -1.5\,\mathrm{mm}$ in the near station, $y < -1\,\mathrm{mm}$ in the far station.

To describe the beam halo in colliding bunches with the unpaired isolated hits, the number of hits in unpaired events needs to be scaled to the number of beam halo hits in colliding bunches. As the beam halo distributions in unpaired isolated events have similar shapes as the beam halo distributions in colliding bunches, the scale factor can be calculated from the beam halo control region.

Samples	$N_{\text{beam halo}}$	N_{data}	beam halo level
Events passing shower removal selection	9206	30716	30 %
Golden events	8723	32044	27 %

Table 2. Beam halo level in data.

$$(\frac{N_{\text{near paired}}(y{<}-1.5\text{ mm})}{N_{\text{near unpaired}}(y{<}-1.5\text{ mm})}+\frac{N_{\text{far paired}}(y{<}-1.5\text{ mm})}{N_{\text{far unpaired}}(y{<}-1.5\text{ mm})})/2$$

It is calculated as the average value of the near station and the far station instead of treating the two stations separately because each track in the near station is matched with a specific track in the far station after the shower removal selection applied. If the two stations are treated separately, the number of beam halo tracks in the two station would not be equal any more, it is better to keep the tracks matched. The value of averaged scale factor is very close to the values of the scale factors in the near station and the far station ($< 2\%$ difference), there is no risks of getting a different conclusion when the two stations are treated separately. The number of tracks in unpaired isolated events in data samples passing the shower removal selection after scaling is equal to number of background events, i.e.:

$$N_{\text{background}} = 9206$$

in Eq. 24. The number of tracks in colliding events in data samples passing the shower removal selection is 30716, so the beam halo background takes up 30 % of the tracks measured by the AFP detector. As a cross check, the same work was also done on golden events, the fitting results are shown in Table 2. The beam halo background takes up 27 % of the golden samples. The level of beam halo background got from golden samples is a little lower than the level got from samples selected by the shower removal selection. However, the golden events selection is over simplified, it is clear that the model describes data distributions better in shower removal samples, see Fig. 30. So the result got from shower removal selection is more reliable, the beam halo level got from golden samples is a cross check of the final result but can not be used as the final result.

5 Radiation Environment at the AFP Stations

The AFP detector will be operated during runs with a high pile-up, and as the detectors and the electronics have some limitation on the radiation, it is necessary to study the radiation environment at the AFP station. Such study was done using full Geant4 simulation [13], we repeated the study on simulation and also did it on data took at high pile-up to compare with the simulation results.

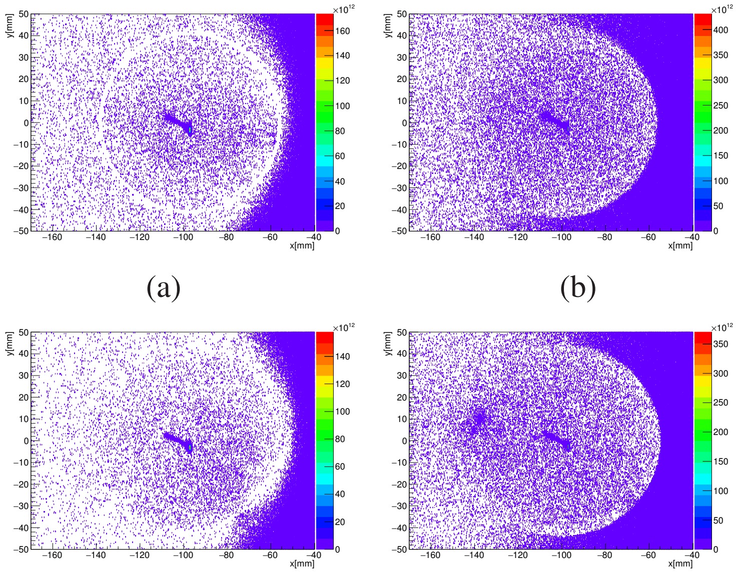

(a) (b) (c) (d)

Figure 31. Hit maps in the vacuum sensors, (a) near station on A side, (b) far station on A side, (c) near station on C side, (d) far station on C side. The highest density region is at the position of the beam center, the circle corresponds to the wall of the 80 mm diameter beam pipe.

5.1 GEANT4 Simulation of Radiation Environment at AFP

To study the particles near AFP, vacuum sensitive detector volumes are added 275 mm in front of every AFP station, which are very thin and covering the AFP stations. It only records the hits but not brings additional effects since the material is vacuum. The Monte Carlo samples used for this study are minimum bias samples generated by Pythia8, including non-diffractive, elastic scattering, single diffractive, double diffractive and central diffractive processes with a total cross section of 108 mb. The optics used in these simulation was the designed LHC optics in the first part of data taking in 2016. The following simulation results were all scaled to 100 fb^{-1}. Fig. 31 shows the hits recorded by vacuum sensors. Most of the particles are protons and electrons, two regions can be distinguished in the hit maps: the region near the beam center together with a high fluence central 'line' at the left side of the beam center, dominated by high energy protons; the region outside this high fluence region, dominated by e^+/e^- pairs. The fluence of high energy protons raises significantly with the distance to the beam center. Fluence of different positions are listed in Table 3. The electronics closest to the beam center is FE-I4 chip on the 3D silicon sensors, where the fluence of high energy proton is smaller than $1 \times 10^{15}/\mathrm{cm}^2$, still below the levels expected for the ATLAS IBL detector [10]. The second closest electronics is the PA-a used for ToF read-out. Other electronics are located at the tunnel floor. The high energy proton fluence at the position where these electronics are located is very small, but these place can still get some electrons. Most of the electrons do not have high energy (<10 MeV), but some of the electrons energy can reach to 100 MeV. The effect of electrons is not very significant compare to the effect of high energy hardons. From the

Position	2 mm from the beam	5 cm from the beam	Tunnel Floor
Electronics type	3D sensor, FE-I4	PA-a	PA-b, CFD, HPTDC
High energy protons fluence	$< 1 \times 10^{15}/\mathrm{cm}^2$	/	/
Electrons fluence	$< 2 \times 10^{15}/\mathrm{cm}^2$	$< 5 \times 10^{14}/\mathrm{cm}^2$	$< 1 \times 10^{11}/\mathrm{cm}^2$
Dose of electrons	< 55 kGy	< 14 kGy	/

Table 3. Particle fluence integrated over 100 fb^{-1}.

electron energy deposition in the silicon sensor, the peak of energy deposited in 0.23 mm material is 10 keV, the dose of electrons at the positions of electronics are listed in Table 3.

5.2 Radiation in High Pile-up Environment

It is necessary to study the high pile-up radiation environment with data because simulations do not cover all picture. The AFP participated in a high pile-up run in 2016, Run 310574, with 1.85 pb^{-1} integrated luminosity. The pile-up of this run was approximately 33. The effect of radiation mainly depends on two factors: high energy hardon fluence and dose. Fig. 32 shows the hit maps of all the silicon sensors, the numbers were scaled to hit rate per second. The number of hits in the last sensor in the far station is about 3 times of the number of hits in the first sensor in the near station. To estimate the maximum fluence, the shower particles have to be taken into account even though most of the showers are low energy electrons. High energy protons usually can have clear signals in all of the sensors, the amount of showers in the first sensor in the near station is the smallest, so the hit rate in the first sensor in the near station is the closest to the hit rate of high energy protons. The hit rate in first sensor in the near station was used to estimate high energy proton fluence, all of the shower particles were assumed as high energy protons.

Based on the hit rate of the first sensor in the near station on C side, we calculated the highest fluence and dose. The fluence got from simulation was integrated over 100 fb^{-1}, to compare data and simulation, the highest hit rate in data was also scaled to fluence integrated over 100 fb^{-1}.

$$\mathrm{fluence}_{\mathrm{max}} = \mathrm{HitRate}_{\mathrm{max}} \times 60\ \mathrm{s} \times 63 \times \frac{100\mathrm{fb}^{-1}}{1.85\mathrm{pb}^{-1}} \times \frac{1\mathrm{cm}^2}{\text{pixel size}} = 1.09 \times 10^{15}/\mathrm{cm}^2$$

In this equation, 60 s is the average time of one lumiblock data, Run 310574 contains 63 lumiblock with integrated luminosity of 1.85 pb^{-1}, so the total time is 60×63 s. $\mathrm{HitRate}_{\mathrm{max}}$ is the maximum hit rate on a pixel, to get the fluence in the unit of per centimeter square, it was scaled $\frac{1\mathrm{cm}^2}{\text{pixel size}}$. The result $1.09 \times 10^{15}/\mathrm{cm}^2$ agrees with the number got from simulation. The maximum fluence in all of the pixels in the near station on C side is $1.77 \times 10^{15}/\mathrm{cm}^2$, still below the levels tested by the IBL detector. Another factor that can have effect is dose, it is defined as the deposited energy divided by mass. Here it can be calculated by the deposited energy in a pixel divided by the mass of the

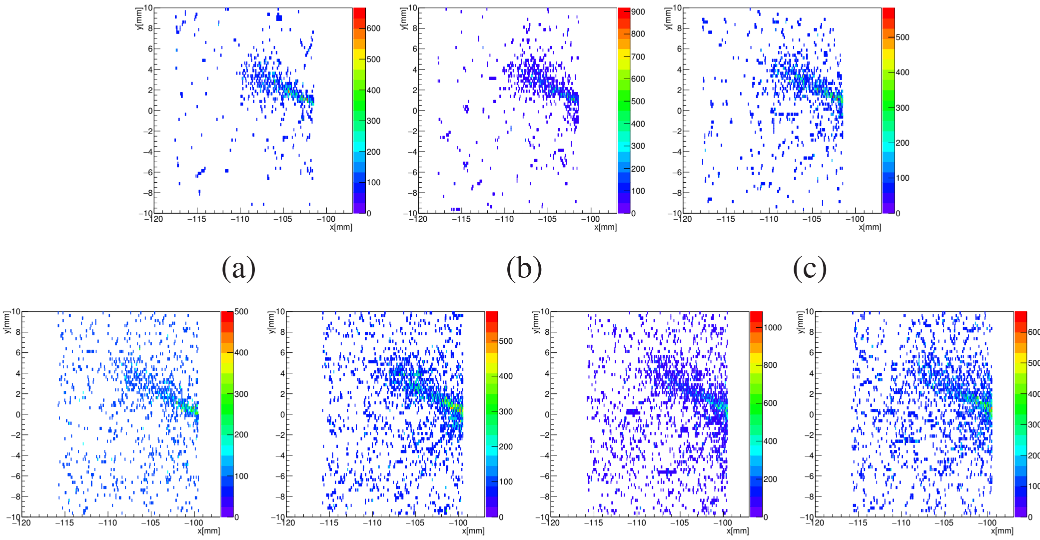

(a) (b) (c)

(d) (e) (f) (g)

Figure 32. Hit maps of (a) the first sensor in the near station, (b) the second sensor in the near station, (c) the third sensor in the near station, (d) the first sensor in the far station, (e) the second sensor in the far station, (f) the third sensor in the far station, (g) the forth sensor in the far station. Got from Run 310574 data.

pixel, the maximum dose got from Run 310574 data was 1268.23 kGy at 100 fb^{-1}, nearly twice of the result ($< 700\mathrm{kGy}$) got from the study did in AFP Technical Design Report [13].

The ToF detector works by detecting the Cherenkov light caused by particles to measure arriving time, it has a limitation on the maximum number of hits. The number of hits that ToF gets can be studied with the hit map of the last sensor in the far station as the ToF detectors are installed in the far station, after the silicon tracker. As described in Sect. 3.1.3, the ToF detector has four groups of trains cover fully the silicon tracker, the width of the bars are 2 mm, 4 mm, 5 mm, 5.5 mm from train 1 to train 4. The fraction of hits on the bars in each train is 21.3 %, 34.6 %, 27.6 %, 16.5 %, as shown in Fig. 33, the width of the trains increased with the distance to the beam center to make the working time of the bars not too different. Train 2 has the highest hit rate, the total hit rate on a sensor is about $3 \times 10^5\ \mathrm{s}^{-1}$.

6 Conclusion

This thesis describes the study based on the full Geant4 simulation of the AFP detector and an estimation of the beam induced backgrounds measured by the AFP detector.

The following changes I had to make: 1) the material in the forward region mother volume was changed from low density vacuum to vacuum with 0 density to make simulation works in the new Athena release; 2) the material in the forward detector envelope was changed from air to vacuum to make simulation faster. The first change was forced by a problem in Geant4, a tracking process stuck when a low energy electron meets low den-

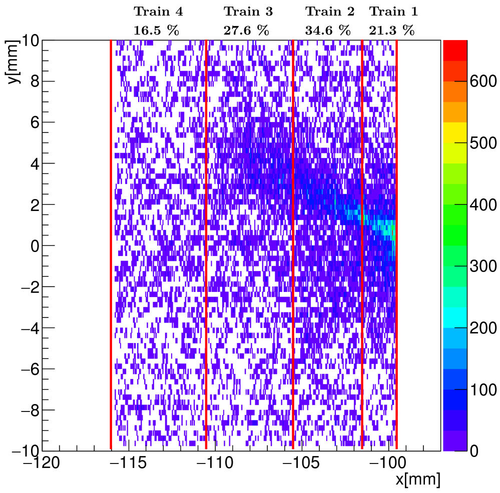

Figure 33. Hit rate on ToF bars, the fraction of hits on each bar are marked in the plot.

sity vacuum. The second change was caused by a remaining problem in simulation: to avoid overlapping volumes, the beam pipe was cut off near the AFP stations in simulation. As a result, the gap was filled with air defined in the forward detector envelope. Beside this gap, other parts of the forward region are vacuum. In the real accelerator, the region outside of the beam pipe are all filled with air, filling only these gaps with air dose not describe the real environment, and simulating showers caused by air only makes simulation more time consuming.

However, the place filled with air in reality was set to be filled with vacuum, some materials like the cooling system were also not implemented in simulation, so some sources of showers caused by real materials are not simulated. From my observation in simulation, very few events (smaller than 4%) were affected by the air out of the beam pipe, when the showers caused by air affected the hits on the sensors, the event usually had several hundred hits or even more than one thousand hits. Such events with too many shower hits are not processes with interest and the showers will be removed before physics analysis no matter they are caused by existing material or not existing material, so it is not needed to spend a lot of time simulating them.

The AFP geometry packages were finished based on an old design, I updated the AFP geometry packages to the correct geometry.

A shower removal selection was developed, it could remove shower tracks effectively and over 90 % of the single diffractive events have at least one track can pass the selection based on the tests using simulation.

With the full Geant4 simulation, I produced single diffractive Monte Carlo samples and minimum bias Monte Carlo samples using Pythia8 as the generator. Data has a region with hits where Monte Carlo samples do not have, the hit distribution in this region has similar kinematics as beam halo: the peak of track y-position distribution is at the position of the beam center.

By requiring events passing the unpaired isolated trigger, I selected a pure beam halo sample from data. The unpaired isolated events in this beam halo sample can be used to describe the beam halo in colliding events. I used the track y-position distributions as the fitting model. Beam halo takes up 30 % of the total number of tracks measured by the AFP detector.

The processes we studied are beam induced background, it is background of diffractive processes. So I implemented a method to selected single diffractive events in data. The logic is to require the MBTS on the opposite side of the side where a proton was detected had signals. It has two possible ways to be achieved, require the MBTS trigger fired or require the MBTS inner modules had signals. The first way can select much more events than the second way, but the single diffractive samples selected by the second way is purer than the sample selected by the first way. These single diffractive samples selected from data contain much less tracks in the region dominated by beam halo, prove from another way that these tracks are caused by beam induced background.

The Monte Carlo samples used for beam induced backgrounds study were also used to estimate the radiation environment at the AFP stations. The method used in this radiation environment analysis was got from the AFP Technical Design Report [13]. I repeated the analysis on Monte Carlo samples that the AFP group did. I also studied the radiation environment with real data taken in a high pile-up run. The results got from simulation were compared to the results got from data. The maximum fluence estimated in simulation agrees with the radiation level in high pile-up data. However, the dose got from data (1268.23 kGy) is nearly twice of the dose got from simulation ($<$ 700 kGy).

Distributions in Monte Carlo agree fairly good with data, the difference is probably caused by the optics used in data taking; it was probably a little different from the designed optics. But the beam induced backgrounds estimation was done using data-driven method, the beam halo part in data agrees well with the model. The difference between Monte Carlo and data dose not affect the result.

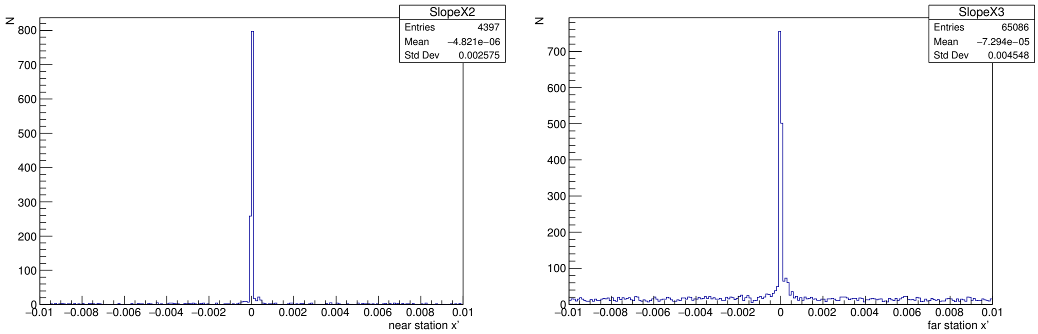

Figure 34. Reconstructed slope distributions of single diffractive Monte Carlo, the near station (left), the far station (right).

A Shower Removal Selection Cuts

The requirements of the shower removal selection are:

- it can remove showers effectively,
- most of the single diffractive proton tracks should be able to pass the selection.

Two cuts are used at step 2(a) in the shower removal selection:

$$\sqrt{(x_{far} - x_{near})^2 + (y_{far} - y_{near})^2} < 2.4 \text{ mm}, |x'_{far} - x'_{near}| < 0.002.$$

The value of the first cut comes from the slope of diffractive protons (90-160 μrad). The far station is about 12 m from the near station, a track with slope of 200 μrad has 2.4 mm offset on the $x - y$ plane between the near station and the far station. Most of the single diffractive proton tracks have smaller slope so they should be able to pass the selection. The second cut comes from the x-slope distributions of single diffractive Monte Carlo, viz Fig. 34. This cut is not as important as the first one because tracks with larger than 200 μrad slope are already removed by the first cut. The slope cut works as a double check. More tracks will be able to pass the selection if we use less tight cut but the ability of removing showers will become weaker. These cuts are able to remove showers effectively and more than 90 % single diffractive events have at least one track passing the selection. To prove this, we tested several groups of cuts on single diffractive Monte Carlo. Here are the cuts tested:

1. $\sqrt{(x_{far} - x_{near})^2 + (y_{far} - y_{near})^2} < 4.8$ mm, $|x'_{far} - x'_{near}| < 0.002$,
2. $\sqrt{(x_{far} - x_{near})^2 + (y_{far} - y_{near})^2} < 3.6$ mm, $|x'_{far} - x'_{near}| < 0.002$,
3. $\sqrt{(x_{far} - x_{near})^2 + (y_{far} - y_{near})^2} < 2.4$ mm, $|x'_{far} - x'_{near}| < 0.002$,
4. $\sqrt{(x_{far} - x_{near})^2 + (y_{far} - y_{near})^2} < 1.2$ mm, $|x'_{far} - x'_{near}| < 0.002$.

Fraction of the number of events with tracks passing the selection and the number of events with tracks is 92.0 % for cut 4.8 mm and 3.6 mm, 91.6 % for cut 2.4 mm, 88.1

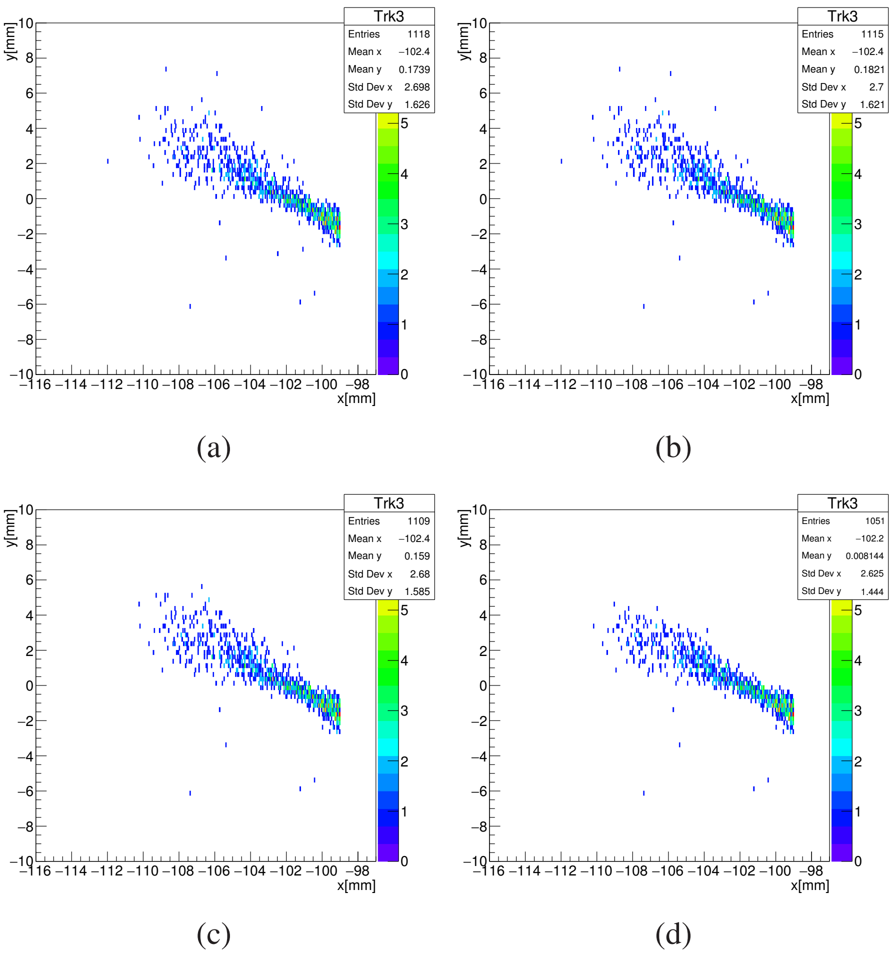

Figure 35. Tracks maps in the far station for single diffractive Monte Carlo. (a) Position offset on the $x - y$ plane smaller than 4.8 mm. (b) Position offset on the $x - y$ plane smaller than 3.6 mm. (c) Position offset on the $x - y$ plane smaller than 2.4 mm. (d) Position offset on the $x - y$ plane smaller than 1.2 mm.

% for cut 1.2 mm. The track maps in the far station for these cuts are shown in Fig. 35. Cut 2.4 mm, cut 3.6 mm and cut 4.8 mm give nearly the same results on single diffractive Monte Carlo, all of them can select clean tracks at high efficiency. Besides let over 90 % of the single diffractive proton tracks pass, the selection also need to remove showers as many as possible, so we choose the smallest value 2.4 mm as the cut. Run 305359 data does not have good enough alignment, so the slope information were not used in the shower removal selection when we compared data and Monte Carlo. Fig. 36 shows the effects of shower removal selection on data.

B Particle Composition at the AFP Stations

As described in Sect. 5.1, most of the particles near the AFP stations are protons and electrons. It can be shown from the pdg ID distributions and proton hit maps. The pdg ID

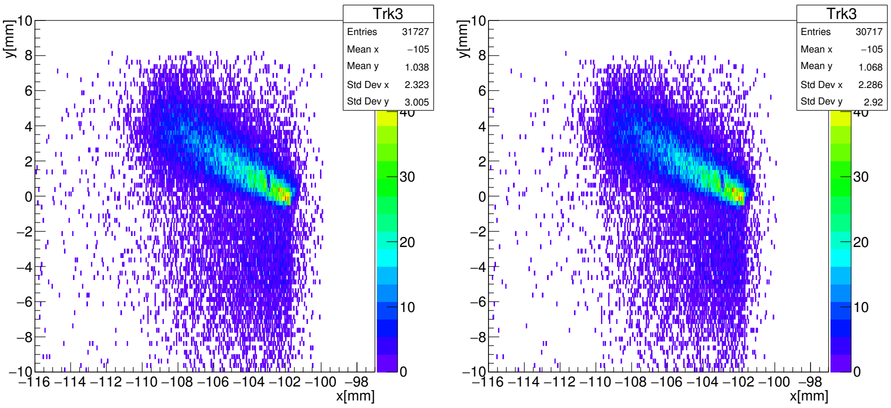

(a) (b)

Figure 36. Tracks maps in the far station for data. (a) Position offset on the $x - y$ plane smaller than 4.8 mm. (b) Position offset on the $x - y$ plane smaller than 3.6 mm.

of proton is 2212, of electron is 11. Fig. 37 shows the particle composition of the vacuum sensors. The two lines (entries) are electrons and protons from left to right. Proton hit maps of vacuum sensors are shown in Fig. 38. Compared to the vacuum sensors shown in Fig. 31, it is clear that the region near the beam center together with a high fluence central line at the left side of the beam center is dominated by protons. Except protons, other particles near the AFP stations are mainly electrons, so particles in the region outside the high fluence region are dominated by electrons.

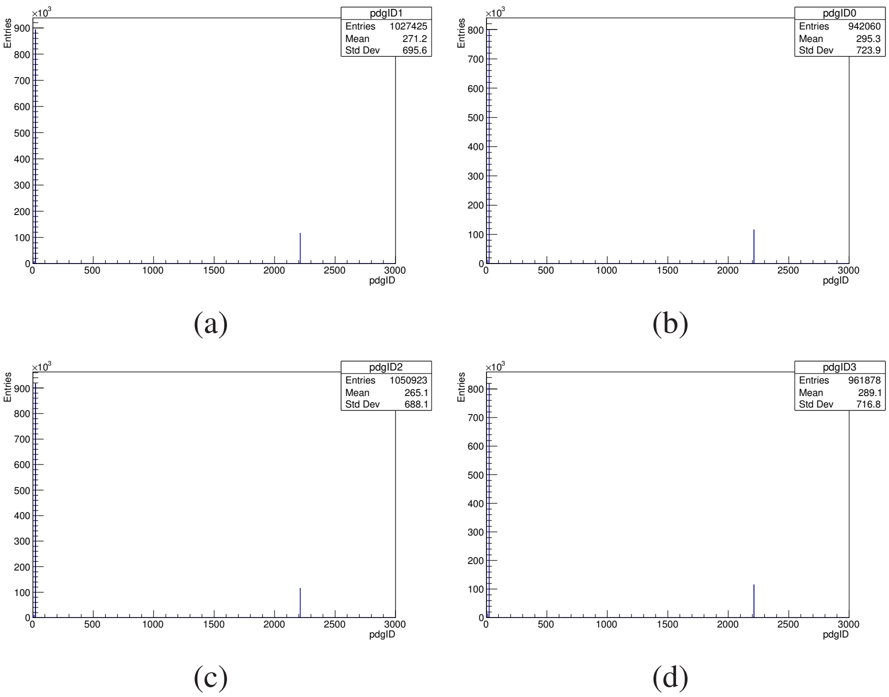

Figure 37. Particle composition of (a) near station on A side, (b) far station on A side, (c) near station on C side, (d) far station on C side.

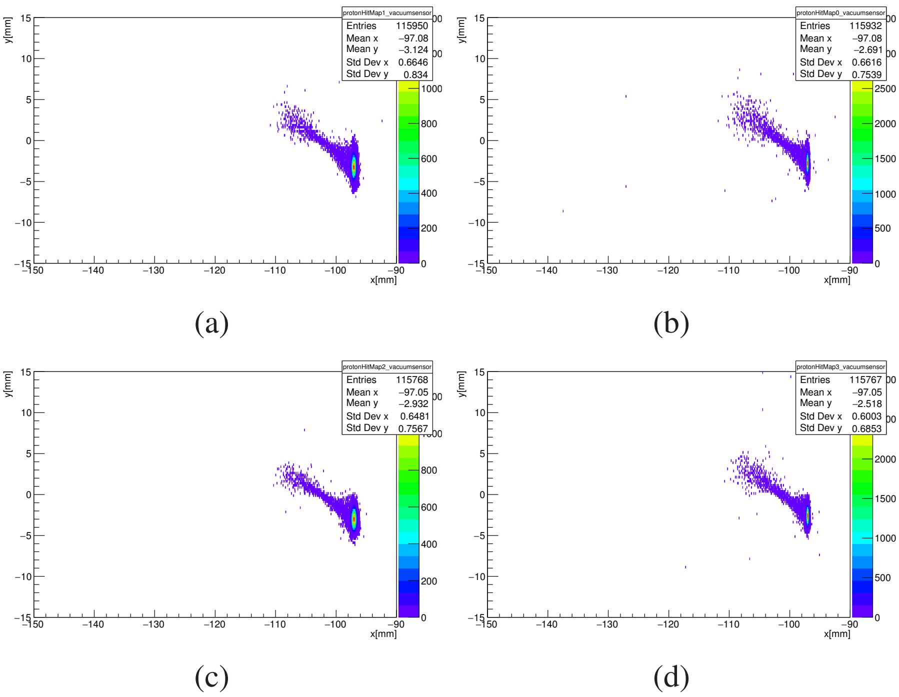

Figure 38. Proton hit map of (a) near station on A side, (b) far station on A side, (c) near station on C side, (d) far station on C side.

Acknowledgement

My thanks belong to my supervisor Tomas Sykora for his excellent supervision; Prof. Yanwen Liu for supporting this project; Grzegorz Gach, Ladislav Chytka, Leszek Adamczyk, Libor Nozka, Maciej Trzebinski, Rafal Staszewski from the AFP Collaboration for their help with the AFP simulation; Riccardo Maria Bianchi for his help with the implementation of the AFP geometry visualization in vp1.

References

[1] Evgene Levin. *An introduction to Pomerons*.

[2] The ATLAS Collaboration. *Characterisation and mitigation of beam-induced backgrounds observed in the ATLAS detector during the 2011 proton-proton run*.

[3] J. Rossbach, P. Schmser. *Basic course on accelerator optics*.

[4] Brning, Oliver Sim (ed.) ; Collier Paul (ed.); Lebrun P (ed.); Myers Stephen (ed.); Ostojic Ranko (ed.); Poole John (ed.); Proudlock Paul (ed.). *LHC Design Report*.

[5] The LHC Study Group Collaboration. *Design study of the Large Hadron Collider (LHC): a multiparticle collider in the LEP tunnel*.

[6] https://lhc-collimation-project.web.cern.ch/lhc-collimation-project/files/Chapter18b.pdf

[7] AFP optics twiki:
https://twiki.cern.ch/twiki/bin/viewauth/Atlas/AFPOptics

[8] TOTEM Collaboration. *CMS-TOTEM Precision Proton Spectrometer, Technical Design Report, September 5, 2014.*

[9] http://www.finetubes.co.uk/uploads/docs/Alloy_316LN.pdf

[10] M.Capeans, G.Darbo, K.Einsweiller, M.Elsing, T.Flick, M.Garcia-Sciveres, H.Gemme, C.Pernegger, O.Rohne, R.Vuillermet. *ATLAS Insertable B-Layer Technical Design Report*

[11] ATLAS IBL Collaboration. *Prototype ATLAS IBL Modules using the FE-I4A Front-End Readout Chip*.

[12] R.Herbst, R.Claus, M.Freytag, G.Haller, M.Huffer, S.Maldonado, K.Nishimura, C.OGrady, J.Panetta, A.Perazzo, B.Reese, L.Ruckman, J.G.Thayer, M.Weaver *Design of the SLAC RCE Platform: A General Purpose ATCA Based Data Acquisition System*.

[13] L.Adamczyk, E.Banas, A.Brandt, M.Bruschi, S.Grinstein, J.Lange, M.Rijssenbeek, P.Sicho, R.Staszewski, T.Sykora, M.Trzebiski, J.Chwastowski, K.Korcyl. *Technical Design Report for the ATLAS Forward Proton Detector*

[14] Forward region simulation packages:
https://gitlab.cern.ch/atlas/athena/tree/master/ForwardDetectors/ForwardSimulation

[15] Geant4 website:
geant4.cern.ch

[16] AFP Geometry model package:
https://gitlab.cern.ch/atlas/athena/tree/master/ForwardDetectors/AFP/AFP_GeoModel

[17] Visualization Point 1 website:
http://atlas-vp1.web.cern.ch/atlas-vp1/home/

[18] https://indico.cern.ch/event/321214/contributions/744366/attachments/620295/853529/ATL-COM-

[19] V. Cindro et al., JINST 3, P02004 (2008).

[20] Antonio.Sidoti. *Minimum Bias Trigger Scintillators in ATLAS Run II*

[21] A. Sidoti *ATLAS Minimum Bias Trigger Scintillator Upgrade for LHC RunII*
https://cds.cern.ch/record/1664105/files/ATL-TILECAL-SLIDE-2014-053.pdf